



## Master in Computational Colour and Spectral Imaging (COSI)



# Data Architecture and Design of *in-vivo* Neurosurgical Hyperspectral Image Database

Master Thesis Report

Presented by  
Gemal Hamid Hisuin

and defended at the  
Norwegian University of Science and Technology

September 2022

*Academic Supervisors:*

1. Dr. Joni Hyttinen, PhD, University of Eastern Finland, Finland
2. Dr. Kiran Raja, Associate Professor, Norwegian University of Science and Technology, Norway
3. Dr. Antti-Pekka Elomaa, PhD, Neurosurgery resident, Kuopio University Hospital/ University of Eastern Finland, Finland
4. Sami Puustinen, B.M./PhD st., Kuopio University Hospital/ University of Eastern Finland, Finland

*Jury Committee:*

1. Dr. Damien Muselet, Assistant Professor, University of Jean Monnet, France
2. Professor José Manuel Benítez, Professor, University of Granada, Spain

Submission of the thesis: 10<sup>th</sup> August 2022

Day of the oral defense: 1<sup>st</sup> September 2022

# Abstract

In recent years, the use of hyperspectral imaging (HSI) for microneurosurgical applications has been introduced. One of the most significant challenge that researchers and neurosurgeons face when developing or applying hyperspectral methods for neurosurgical applications is the absence of publicly available hyperspectral data with appropriate metadata, anatomical accuracy, patient characteristics, and reflectance properties of brain tissues and tumor. This work's goals were to create an application for visualizing the reflectance spectral signature of various tissue and tumor characteristics using a gold standard dataset collected by the research group, as well as to assess the focus quality of the band images. Using this data, a reference of brain tissue and tumor spectral signatures was created, which was subsequently utilized to identify more than 9 distinct tissue classes and tumors that may be used to delineate brain tumors during intraoperative neurosurgical operations. For improved accessibility and usability, a data architecture was designed to illustrate the flow of microneurosurgical data acquisition, storage, processing, and display. A database system with a web-frontend was developed to store and display hyperspectral images and complement the dataset with magnetic resonance and computed tomography images. The hyperspectral imaging clinical database can also be utilized to further develop HSI algorithms and machine learning-based neurosurgical applications.

In addition, out-of-focus in the acquired spectral images is one of the main drawbacks in the brain tissue and tumor delineation and identification. And, to evaluate the focus of those images, quality evaluation techniques that are known to provide good results with RGB images were tested on the band images of our hyperspectral images. As a result, this study examines a blur-based no-reference image quality assessment algorithms for evaluating the sharpness of the band images. A hyperspectral image dataset was created for this purpose by blurring the same spectral band image with different blur levels of gaussian filter, one acquired between 500 nm and 950 nm and the other between 500 nm and 900 nm, and each independent wavelength was analyzed. Perceptual Sharpness Index (PSI) focus assessment method performed better in the spectral bands of neurosurgical images. Also, focus differences were noticed in the final wavelength range between 900 nm and 950 nm, even though, the results show focus consistency in the acquired dataset between 500 nm and 900 nm.

# Acronyms

<b>BIBE</b>	<b>B</b> lind <b>I</b> mage <b>B</b> lur quality <b>E</b> valuator
<b>BRISQUE</b>	<b>B</b> lind/ <b>R</b> eferenceless <b>I</b> mage <b>S</b> patial <b>Q</b> uality <b>E</b> valuator
<b>CSS</b>	<b>C</b> umulative <b>S</b> pectral <b>S</b> ignature
<b>CT</b>	<b>C</b> omputed <b>T</b> omography
<b>DICOM</b>	<b>D</b> igital <b>I</b> maging and <b>C</b> OMmunications in <b>M</b> edicine
<b>EMCCD</b>	<b>E</b> lectron <b>M</b> ultiplying <b>C</b> harge <b>C</b> oupled <b>D</b> evice
<b>GGD</b>	<b>G</b> eneralized <b>G</b> aussian <b>D</b> istribution
<b>GUI</b>	<b>G</b> raphical <b>U</b> ser <b>I</b> nterface
<b>HELICoiD</b>	<b>H</b> yp <b>E</b> rspectra <b>L</b> <b>I</b> maging <b>C</b> ancer <b>D</b> etection
<b>HSI</b>	<b>H</b> yperspectral <b>I</b> maging <b>S</b> ystem
<b>HVS</b>	<b>H</b> uman <b>V</b> isual <b>S</b> ystem
<b>IQA</b>	<b>I</b> mage <b>Q</b> uality <b>A</b> ssessment
<b>JNB</b>	<b>J</b> ust- <b>N</b> oticable <b>B</b> lur
<b>KUH</b>	<b>K</b> uopio <b>U</b> niversity <b>H</b> ospital
<b>LED</b>	<b>L</b> ight <b>E</b> mitting <b>D</b> iode
<b>LPC</b>	<b>L</b> ocal <b>P</b> hase <b>C</b> oherence
<b>MF</b>	<b>M</b> edian <b>F</b> ilter
<b>MLV</b>	<b>M</b> aximum <b>L</b> ocal <b>V</b> ariation
<b>MRI</b>	<b>M</b> agnetic <b>R</b> esonance <b>I</b> maging
<b>MSS</b>	<b>M</b> ean <b>S</b> pectral <b>S</b> ignature
<b>NR-IQA</b>	<b>N</b> o- <b>R</b> eference <b>I</b> mage <b>Q</b> uality <b>A</b> ssessment
<b>NSS</b>	<b>N</b> atural <b>S</b> cene <b>S</b> tatistics
<b>PCA</b>	<b>P</b> rincipal <b>C</b> omponent <b>A</b> nalysis
<b>PLCC</b>	<b>P</b> earson <b>C</b> orrelation <b>C</b> oefficient
<b>PSI</b>	<b>P</b> erceptual <b>S</b> harpness <b>I</b> ndex
<b>RGB</b>	<b>R</b> ed <b>G</b> reen <b>B</b> lue
<b>sCMOS</b>	<b>s</b> cientific <b>C</b> omplementary <b>M</b> etal <b>O</b> xide <b>S</b> emiconductor
<b>SRCC</b>	<b>S</b> pearman's <b>R</b> ank <b>C</b> orrelation <b>C</b> oefficient
<b>SVM</b>	<b>S</b> upport <b>V</b> ector <b>M</b> achine
<b>VNIR</b>	<b>V</b> isible and <b>N</b> ear <b>I</b> nfra <b>R</b> ed

# Contents

<b>1</b>	<b>Introduction</b>	<b>1</b>
1.1	Aim and Objective . . . . .	4
1.2	Contributions . . . . .	6
1.3	Structure of the report . . . . .	6
<b>2</b>	<b>Literature review</b>	<b>9</b>
2.1	Acquisition techniques of neurosurgical hyperspectral images . . . . .	9
2.1.1	Spectral scanning . . . . .	10
2.1.2	Spatial scanning . . . . .	10
2.1.3	Snapshot acquisition . . . . .	11
2.2	Hyperspectral imaging for microneurosurgery applications . . . . .	13
2.3	Standardization of spectral imaging for microneurosurgery . . . . .	13
2.4	Database of spectral-based microneurosurgery . . . . .	15
2.5	Blur-specific quality measurement of microneurosurgery spectral images . . . . .	16
2.6	Conclusion . . . . .	17
<b>3</b>	<b>Methodology</b>	<b>19</b>
3.1	Dataset . . . . .	19
3.1.1	Intraoperative microneurosurgical HSI system . . . . .	20
3.1.2	Phases of HSI acquisition . . . . .	21
3.2	Data pre-processing . . . . .	23
3.2.1	Anatomical annotation and labeling . . . . .	24
3.3	Neurosurgical HSI system and database architecture . . . . .	24
3.3.1	System functionality . . . . .	24
3.4	Blur-specific quality assessment of spectral band images . . . . .	27
3.4.1	NR-IQA Algorithms . . . . .	28
3.4.2	Support Vector Machine (SVM) for sharpness classification of band image . . . . .	34

## CONTENTS

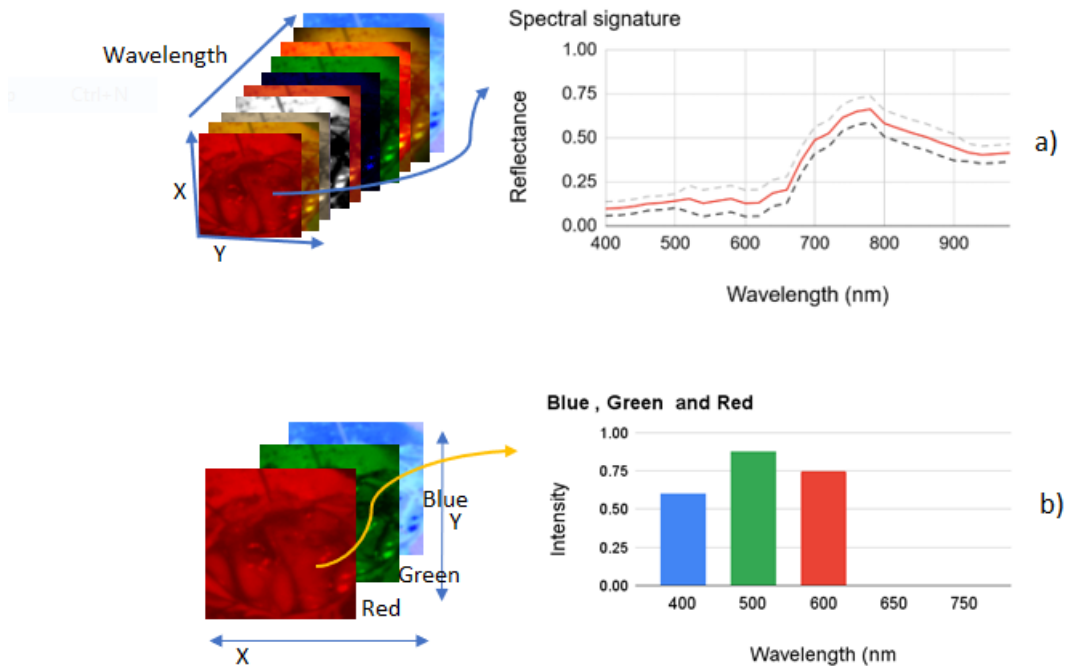
<b>4</b>	<b>Results</b>	<b>37</b>
4.1	Database architecture . . . . .	37
4.1.1	Imaging case data classes . . . . .	37
4.1.2	Tissue classes and class features . . . . .	39
4.2	System architecture and functionality . . . . .	41
4.3	Blur-specific quality assessment of the hyperspectral image bands .	45
4.3.1	Blur-specific quality estimation with SVM . . . . .	50
<b>5</b>	<b>Discussion</b>	<b>53</b>
<b>6</b>	<b>Conclusions</b>	<b>55</b>
<b>7</b>	<b>Limitations and Future Works</b>	<b>57</b>
<b>A</b>	<b>Appendix</b>	<b>59</b>
	<b>Bibliography</b>	<b>65</b>
	<b>List of Figures</b>	<b>71</b>
	<b>List of Tables</b>	<b>75</b>

# 1 | Introduction

Originally developed for use in remote sensing applications, hyperspectral imaging (HSI), which is also known as imaging spectroscopy, has recently been explored for various applications in a variety of fields, including astronomy (Hege et al., 2004), cultural heritage (Marcello et al., 2020), surveillance and target identification (Yuen and Richardson, 2010), biology (Pisani et al., 2013), and agriculture (Dr. Dr. Dale et al., 2013). The spectral imaging approach collects electromagnetic radiation from a scene in the range of 200 nm to 2500 nm using spectrometer. The collected electromagnetic radiation comprises a three-dimensional data cube with both spatial and spectral dimensions. Contrary to RGB imaging technology, which can only collect data in three channels of red, green, and blue spectrum, spectral imaging technology allows us to capture and store information in more than three channels of band for a given scene. Figure 1.1 shows how RGB images and spectral images are represented.

Spectral imaging allows for the non-invasive examination of brain tissue characteristics during brain surgery, and recent advancements in spectral device speed and size have made it possible for these technologies to be used in disease diagnosis and treatment methods such as image guided surgery (Blair et al., 2019). Potentially useful applications of HSI in the medical field have been made possible because of recent developments in advanced imaging technology, image analysis methods, and computational power.

Certain types of brain tumors infiltrate the surrounding healthy brain tissues, and as a result, the boundaries of brain tumors are unclear and difficult, if not impossible, for a surgeon to identify with only their bare eyes (Fabelo et al., 2019). There is no doubling of tissues in the brain, in contrast to what happens in the majority of other organs, when the tumor is often removed together with a block of healthy tissue (Fabelo et al., 2019). It is essential to get a precise diagnosis of the tumor margins in the brain in order to remove the minimum amount of healthy tissue possible. Considering that, spectral image analysis could be used to reliably identify malignant tumors during surgery in these kinds of situations (Fabelo et al., 2018, 2019).



**Figure 1.1:** a) Data cube representation b) RGB representation. The data cube contains spatial and spectral data. On the left is a pixel’s spectral reflectance curve. On the right, the RGB representation contains three bands for red, green, and blue wavelengths, and a pixel’s intensity curve from the RGB scene.

HSI cameras can be designed to function in a number of different wavelength ranges, including the ultraviolet (200–380 nm), visible range (380 - 780 nm) and the near-infrared (700–2500 nm) (Lu and Fei, 2014). Some hyperspectral systems employ two cameras with varying wavelength ranges, but others employ only one camera for a shorter wavelength area (VNIR=500-1000 nm).

Multiple imaging modalities are utilized to guide neurosurgical tumor removal (Fabelo et al., 2019). Intraoperative neuronavigation devices employ preoperative image data to guide surgery in real time. Intraoperative MRI eliminates brain shift by monitoring tissue resection (Fabelo et al., 2019), but it demands an MRI-compatible operating room and prolongs surgery (Gandhe and Bhawe, 2018). Another modality option could be ultrasound imaging, which is cheap and undisturbed by brain displacement, but typically has poor image quality due



to/and low resolution. Spectral imaging, on the other hand, is a non-contact, label-free, safe for the patient imaging modality that can have high spatial or spectral resolution. Considering these options, spectral imaging could be the better imaging modality to use during surgery provided that spectral image analysis can be performed near-realtime.

The majority of intraoperative HSI teams in the field of medical science are associated with the abdominal cavity (Ortega et al., 2019a). Jansen-Winkeln et al. (2019) employed HSI instead of macroscopic examination to identify the resection margin of colorectal resections while they were dealing with surgical complications in the intestine. In HELICoiD project (Fabelo et al., 2019), a system equipped with two hyperspectral cameras is now being developed. The researchers' previous work proved that human brain cancers could well be identified in neurosurgery by making use of hyperspectral imaging technology (Gebejes et al., 2016; Fabelo et al., 2016).

The number of medical applications that make use of hyperspectral imaging has increased over the course of the past few years. When it comes to creating hyperspectral techniques for medical applications, one of the most significant obstacles that researchers must overcome is the lack of hyperspectral medical data that is made available to the public (Fabelo et al., 2019). Despite the volume of research that has been conducted and the growing popularity of open-access ideas, the number of neurosurgical hyperspectral imaging datasets that are freely and publically available is still somewhat restricted. Images of tissue from the brain (Fabelo et al., 2019), oral cavity (Hytinen et al., 2020) and the retina (Styles et al., 2006) are three of the rare medical hyperspectral image collections that are freely available to the public.

In addition, it is possible for images to be distorted in a number of ways, particularly when working with microscopic hyperspectral images (Ortega et al., 2019b). Despite the fact that high-quality HSI cameras are readily available, the majority of HSI applications, such as cancer detection in histology samples, require images to be particularly sharp (Ortega et al., 2020). For that matter, sharpness image quality assessment (IQA) is an essential method for spectral images as there has not been an ideal method for assessing the quality of the spectral band images from focus perspective.

It has also been a long-standing goal of many researchers to build new imaging systems that utilize the hyperspectral technology in a wide range of scientific domains. HSI technology hasn't contributed to significant business markets, possibly

because its infrastructure of elemental approaches isn't as developed as RGB color imaging. For spectral technology, methodologies such as image sensor devices and image format are not commonly standardized. Therefore, it would be challenging for business corporations to adapt spectral technology to their products, as they would need to develop all of the elemental approaches independently.

The worldwide standard for storing and exchanging data for medical images and related information is DICOM in the field of medical imaging. It specifies the formats for medical images and the quality required for clinical usage, but the standard does not currently support spectral images. The ENVI image file format which is a spectral image format that is used for practical areas including in satellite and airplane remote sensing data can store the parameters of the acquired information in hdr and raw files. If the ENVI file format is going to be used for medical applications to record spectral information it could be a possible source of error and might make analyzing and comparing the images challenging as ENVI requires to be stored in more than one file extension formats (hdr and raw). In light of this, there needs to be a standardized image format for medical HSI that can be used in a manner that is consistent across the board by all spectral applications that are now being used in the field.

## 1.1 Aim and Objective

The study that is presented in this thesis aims to design a data architecture, to create a spectral database, and to develop system functionality for hyperspectral imaging which will be primarily useful for intraoperative microneurosurgical applications. Additionally, a technique for evaluating the sharpness of hyperspectral microscopic images and the relationship between wavelength and focus of the band images is studied during this work. As a consequence of this, inquiries have been made regarding the manner in which this work might be utilized to the advantage of neurosurgical medical applications and the manner in which the data architecture workflow of the application that is planned should be established.

**Significant problems pertaining to this topic includes the following:**

Question 1: How should microneurosurgical hyperspectral data be gathered and included into the neurosurgical image database?

Question 2: Which types of information obtained from hyperspectral imaging should be kept in a database so that they may be used as a reference for potential future neurosurgical procedures?

Question 3: Is there a way to assess the quality/focus of the spectral band images?

Question 4: Is there a relationship between the wavelength, chromatic aberration and the focus of the spectral band images acquired with the given spectral camera at KUH?

**In light of the characteristics of the HSI data and the aim of the study, the following hypotheses have been formulated for the purposes of this investigation:**

1. Microneurosurgical hyperspectral information might be stored and shared via a database, and data collection for this type of image could be standardized.
2. It is possible to have predetermined HSI data information that can be utilized as a reference for future intraoperative neurosurgery.
3. The focus level of spectral images can potentially be evaluated with the use of a computer algorithm.
4. There is a correlation between wavelength, chromatic aberration and sharpness of the band images.

## 1.2 Contributions

A web-based application was developed during the thesis work. This application will have the capacity to save, retrieve, and analyze neurosurgical hyperspectral images. In addition to databases, the application will be able to display a list of thumbnail RGB reconstruction images, as well as annotated classes, masks, and brain tissue and tumor classes. Furthermore, it will be able to display an averaged spectral signature for each labeled class of the neurosurgical spectral image, such as artery, vein, and blood. In addition, over the course of the work, a no-reference based IQA technique that can be utilized to evaluate the spectral neurosurgical band images gathered at the hospital is tested and experimented, and a relationship between the wavelength of the band images and their sharpness level has been observed. The spectral images can be checked utilizing this quality assessment algorithm prior to being added to the database. And, our work that is presented in this thesis study was accepted for publication in the IEEE 35th International Symposium on Computer Based Medical Systems (CBMS 2022 conference) (Puustinen et al., 2022).

## 1.3 Structure of the report

The structure of this thesis report is divided into six sections. In Chapter 1, we go through the fundamental idea behind hyperspectral imaging

technology, how HSI may be used in medical and neurosurgical applications, the purpose and objective of the thesis, as well as a description of the contribution of the thesis work.

In Chapter 2, a review of the relevant literature is presented, which includes an overview of the design of the HSI database, and techniques for assessing the quality of HSI data.

The discussion of the available dataset features comes first in the methodology section of the thesis report after hyperspectral imaging acquisition techniques in Chapter 3, and is followed by a discussion of the methods and algorithms that were employed throughout the thesis study.

Experiments and the results are discussed in Chapter 4. Following an initial discussion of the working environment, the subsequent explanation of the experiment outcomes is discussed.

Chapter 5 will be a discussion section, and Chapter 6 will be the conclusion section of the report and some prospective enhancements for future advances.

**Chapter 1 | INTRODUCTION**

## 2 | Literature review

A literature review in related domains has been conducted to have the existing understanding which can help to develop a data architecture of the HSI system for neurosurgical application and to analyze NR-IQA methods that can be utilized for evaluating the raw band images acquired using the specified HSI camera. The literature review primarily concentrated on the acquisition methods used to gather spectral data, the use of spectral imaging in neurosurgery, the standardization of spectral image format and spectral data exchange in the medical field, the existence of neurosurgical databases, and finally the evaluation of focus level of the spectral band images.

### 2.1 Acquisition techniques of neurosurgical hyperspectral images

Based on the width and the number of spectral bands captured, spectral-based imaging systems can be classified as multispectral, hyperspectral or ultraspectral. But, as "multi", "hyper" and "ultra" do not actually have precise definitions, there have also been calls to drop these adjectives in favor of more scientifically sound terminology. The suggested terms were imaging spectroscopy and spectral imaging (Polder and Gowen, 2020). In this paper, the terms "imaging spectroscopy" and "hyperspectral imaging" will be used interchangeably to refer to the same concept. Lu and Fei (2014) provide an overview of the fundamental camera procedures used to build the spectral datacube that can be used to represent various tissue classes and tumor types. These device-based methods are classified as spatial scanning, spectral scanning, and snapshots. Table 2.1 compares the acquisition technique, number of spectral bands, target tissue, spatial resolution, and spectral resolution used in different studies in the application and scope of surgical spectral imaging.

### 2.1.1 Spectral scanning

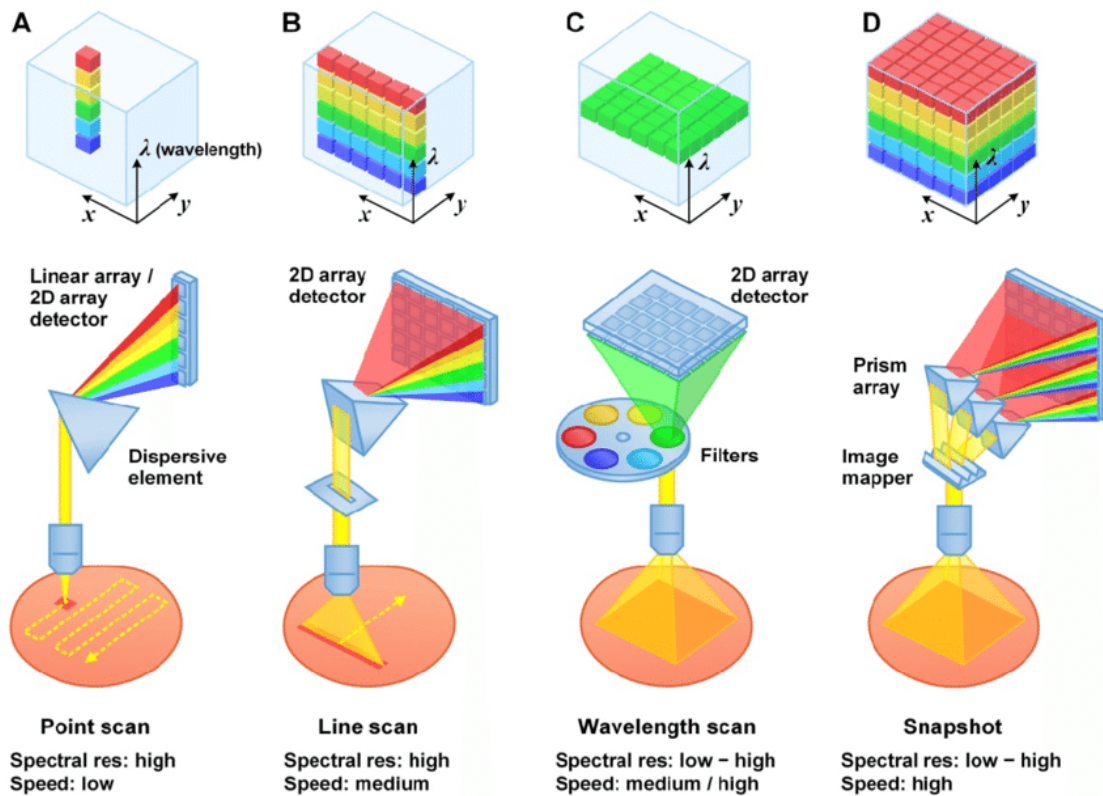
Clancy et al. (2020) states that, spectral scanning has the benefit of being compatible with the existing xenon surgical light sources that are currently in use. Besides that, a proportionally simple detecting hardware can be properly connected to clinical imaging tools. Consequently, filter-based surgical spectral imaging (SSI) devices can be adjusted to be installed on operational microscopes with only slight adjustments and these devices can be placed on a movable arm so that they can be used during imaging operations (Holmer et al., 2018). During prolonged sequences, relative motion between the tissue and the camera can produce artifacts in the datacube; however, this can be corrected after acquisition by utilizing registration techniques (Du et al., 2015).

The increasing presence of light-emitting diodes (LEDs) at a variety of wavelengths has made it possible to develop light-efficient HSI sources (cameras) that are able to switch at a rapid speed and at a minimal cost (Bolton et al., 2018). This has been made possible by the fact that LEDs can emit light at multiple wavelengths. The integration of fluorescence excitation and reflectance measurements is possible with the use of a strobed LED source in conjunction with a good quantum performance device, such as an EMCCD or sCMOS. LEDs have a number of drawbacks, the most notable of which include poor fiber coupling, which makes it challenging to apply them in neurosurgical implementations, and unpredictable spectral resolution over the whole visible and infrared(near) spectral ranges (Ma et al., 2016).

### 2.1.2 Spatial scanning

Spatial scanning implies collecting spectral data from a single point (whisk-broom) or line (push-broom, Figure 2.1(c)). A high level of spectral resolution may be achieved using spectrometers and imaging spectrographs throughout a wide range of wavelengths. The spatial resolution that can be attained is compromised in two ways: first, by the amount of scan lines that are captured, and second, by the restrictions that are caused by any movement in the target tissue. Pushbroom imagers have dispersive optical components, making minimization of device size difficult. Alternatively, advancements including Fabry-Pérot interference filter sensors facilitated to the development of hyperspectral cameras with spectral sensitivity combined along one side of the sensor (Pichette et al., 2017). It is also difficult to match the spatial slices after acquisition and this method is sensitive to motion artifacts, which is another drawback, but it is possible to do motion correction by making use of wide-field images captured with a second camera(Yoon





**Figure 2.1:** Methods for collecting hyperspectral images. Both A and B illustrate spatial scanning. Scan Point (A). Line scan (B). spectral scanning (C). Snapshot (D). Adapted from (Wang et al., 2017)

et al., 2019).

### 2.1.3 Snapshot acquisition

Snapshot imagers are capable of simultaneously recording all three dimensions that make up a datacube. When doing this, it is common practice to distribute the data for both the spatial and spectral dimensions over a single image sensor. The work by Hagen and Kudenov (2013) offers a comprehensive analysis of snapshot imaging systems as well as a comprehensive explanation of the operational concepts behind these systems. Snapshot capture has the drawback of capturing data rapidly at the expense of spatial resolution. This significantly decreases the amount of wavebands that can be utilized in the HSI domain, depending on the approach employed.

Table 2.1: A comparison of existing surgical spectral imaging approaches.

Author	Scan method	Dispersive element	Spectral range (nm)	Spectral resolution	Spatial resolution	Band count	Frame rate (fps)	Target tissue
Ma et al. (2016)	Spectral	Tunable source (multi LED)	530–630	18–33	512 × 512	2	10 (not given)	Brain
Bolton et al. (2018)	Spectral	Tunable source (multi LED)	400–950	11–100	2592 × 1944	13	0.03 (not given)	Skin
Fawzy et al. (2015)	Spectral	Tunable source (filter wheel)	400–760	15	659 × 494	18	15 (2.4 s)	Lung
Lin et al. (2018)	Snapshot	Fibre bundle, spectrograph	460–690	6	1024 × 768	24	2 (500 ms)	Bowel, larynx
Tetschke et al. (2016)	Spatial	Spectrograph	500–1000	5	640 × 480	100–750	0.1 (40 s)	Kidney
Kiyotoki et al. (2013)	Spatial	Spectrograph	400–800	5–10	640 × 480	72	0.06–0.2 (10–90 s)	Stomach, brain, bowel
Ayala et al. (2019)	Spectral	Filter wheel	470–700	20–25	1228 × 1029	8	2.5 (0.18 s)	Bowel, brain

## 2.2 Hyperspectral imaging for microneurosurgery applications

To this day, a few research groups have published neurosurgical HSI reports including (Ruiz et al., 2020; Ebner et al., 2021), but the HELICoiD research group is the only one with publicly available neurosurgical database (Fabelo et al., 2016, 2018). They were able to demonstrate with high sensitivity that hyperspectral imaging can be used to make a distinction between normal hypervascularized tissue, background, brain tissue and tumor. They showed that label-free HSI might be used to guide surgery for brain tumors (Fabelo et al., 2016, 2018). The fact that the HELICoiD system's hardware is bulky and heavy is one of its drawbacks (Fabelo et al., 2016, 2018). Because of this, it is challenging to implement the system into standard in-vivo neurosurgery workflows. Similarly, the amount of data that will be gathered and how it will be used will be restricted. Real-time intraoperative imaging analysis involves high-speed computational processing, and this requires a large training dataset. On the HeliCoid project, however, spectral images were acquired from only 22 patients (36 captures) (Fabelo et al., 2016). As a consequence of this, the overall time required to process an image, which includes the time required for both the capture and the computational processing, ranged from 35.53 to 68.76 seconds, and this is the challenge even after the implementation of a faster processing approach (Fabelo et al., 2018). The majority of these tests had a lengthy HS cube capture and processing time (ranging from 5 to 30 seconds), which is currently the primary barrier to the development of a real-time hyperspectral imaging system that is suitable for intraoperative usage. Given this, future research should consider on developing intraoperative hyperspectral imaging systems that are ideal while yet being practical. These systems should be compatible with existing surgical environments that are extensively utilized and should be able to be adjusted for usage in a variety of surgical procedures. It is important for researchers to establish crucial design aspects in order to facilitate the straightforward incorporation of such a technology into the planned surgical technique.

## 2.3 Standardization of spectral imaging for microneurosurgery

Despite advances in hyperspectral imaging in medical applications, there is still no standard file format or standardization policy that can be used to manage and control spectral imaging data processing within the field. Even DICOM, which is an extensive specification of contextual information, structure, data storage, and

communications protocols for the electronic transfers of therapeutic and diagnostic images and image-related details in the medical field, has yet to include any standardization policy for integrating spectral images in its system.

The CIE 223:2017 standard (Yamaguchi et al., 2017) has addressed a technical report that specifies the core notion of spectral imaging technology and four unique file formats, AIX, JPEG 2000, Spectral Binary, and Natural Vision, are compared and contrasted for standard file format spectral image for different application fields.

Sakamoto et al. (2014) mentioned that Natural Vision (NV) image format has the potential to serve in the same capacity as a spectral data format in the context of biological applications. During their research, they developed a program for managing spectral imaging data and exploratory condition settings within a single file. The tool is flexible, user-friendly, and reduces the likelihood of errors by keeping all of the information concurrently. Additionally, it offers up new ways for supplementary analysis that is associated with databases, and if numerous systems implement the NV image format as the standard for storing and sharing spectral images, researchers will be able to store their spectral images in a central database and compare them to the spectral images of other studies.

Hauta-Kasari et al. (2006) released an architecture for for Spectral Image Browsing, which tackles the difficulty of navigating spectral image archives, which takes into account the issue of transferring images quickly between the host server and the client computer. It is generally agreed that accurate spectral information is not necessary for browsing; nonetheless, enough visual quality is necessary for the images. On the client side, the spectral image can be recreated in order to modify the display filter so that it corresponds to the display that the user desires. The spectral images can be stored on the server in the raw spectral file type or in device independent data types with the support of PCA. If a user has a spectral image and wants to find a comparable image in the spectral image database, one method that the client can use is to first determine the eigenvectors for the spectral image, and then search for images in the database by using the eigenvectors as a filter. This method is useful in situations where the client user already has the spectral image. Because of this, it is possible to search for images that have similar spectral qualities. The results of their analysis indicate that the suggested method of compression is suitable for browsing.

## 2.4 Database of spectral-based microneurosurgery

At this time, there are only a limited number of intraoperative hyperspectral datasets of medical images that are available to the public. Hyttinen et al. (2020) developed the first publicly available oral and dental spectral image database by using spectral cameras to acquire 316 spectral images of human test participants for the oral and dental spectral image database. The data was gathered initially with a HS camera of Nuance EX and then with Specim IQ. The Specim IQ camera has a wavelength range of 400-1000 nm, whilst the Nuance Ex camera has a range of 450-950 nm. Gebejes et al. (2016) recorded a spectral eye video database, and in their study they established a spectral and video cameras enabling collection of a new dataset consisting of 180 spectral eye movement data and 30 spectral images of the eyes of 30 voluntary participants. A thorough collection of the eye's spectral signatures and its surroundings was able to be made possible due to the spectral video that was obtained in the wavelength region of 380-1000 nm and the spectral still imagery that was acquired in the area of 450-950 nm. The features contained in the database can be utilized to construct innovative methods for imaging, training, analyzing, and interpreting eye tracking data.

Fabelo et al. (2019) published the first in-vivo hyperspectral human brain imaging database, and its primary purpose was to investigate the ability of spectral images to detect and classify brain tumors during surgical operations. There is a possibility that the introduction of HSI into an intraoperative imaging guided surgical system will have an immediate impact on the patient's ability to get an accurate diagnosis. Potential benefits include proving complete resection during surgical operations, preventing problems created by the brain motion phenomenon, and providing assurance that the surgery's goals were effectively met. Additionally, confirming complete resection can prevent difficulties caused by the brain movement phenomenon. A data set referred to as the gold standard was created comprising 36 in-vivo human brain images obtained from 22 participants. The images contain labels for the tumor, normal tissue, blood arteries, and other tissue substances. As a result of this, the authors have gathered an initial database that may be utilized to undertake future study in the use of HS data to identify healthy tissues and particular brain tumor, that can provide information to surgeons that could be valuable in increasing the achievements of the surgical treatment.

## 2.5 Blur-specific quality measurement of microneurosurgery spectral images

When it comes to the vast majority of medical HSI applications, including the identification of cancer in histology samples (Meer et al., 2012), sharp images are absolutely necessary. Therefore, focus assessment using image quality assessment (IQA) methods has become an important technique to evaluate the sharpness of the band images. There are three types of objective IQA methods: full reference, no reference, and reduced reference. The no-reference (NR-IQA) method is favoured in blur image applications since ground truth images are not readily available; nevertheless, it is also more difficult.

There are a number of no-reference IQA approaches developed for RGB images, including Blind-Referenceless Image Spatial Quality Evaluator (BRISQUE) (Sun et al., 2015) and Blind Image Blur quality Evaluator (BIBE) (Li et al., 2015a). Nonetheless, when applied to imaging spectroscopy data, the current state of the art of these approaches are relatively not-efficient enough to evaluate the sharpness of spectral band images. The development of non-reference image quality assessment system started with an analysis of particular visual distortions, including noise and blur that are present in images on a regular basis. Quintana Quintana et al. (2021) has applied NR-IQA approaches tested on RGB images to spectral band images between 400 nm to 1000 nm acquired using Hyperspec camera model and spatial scanning push-broom acquisition technique, and they have observed how the different approaches can be used to determine the focus level of the images, and their result shows a low correlation between the focus of band images in the 900 nm to 1000 nm range due to low camera sensitivity. According to (Hou et al., 2020) a number of studies were conducted with the goal of minimizing the interference caused by the many different types of visual distortions. In the framework of their investigations, the vast majority of them developed an integrated IQA method by modeling the human sense of vision and cognitive processes. Image blur, noise, blockiness, and JPEG compression have been the subject of the most studies on image quality assessment for visual distortions.

The process of blurring an image will, in most cases, result in the edges being more visible. As a result, fuzzy estimate algorithms place a primary emphasis on determining the width of the edge. Estimating the edge width in a specific direction is done by several methodologies, such as the one proposed by (Marziliano et al., 2002). The impact of noise and isolated spots may be reduced using a wide variety of IQA approaches, many of which include data fitting and quantization

on image edges. Dijk et al. (2003) presented orthogonal filters to identify edges for each visual scene. These filters evaluate width and intensity of the edges using a Gaussian shape, and then compute the components that are smaller than a predefined threshold to determine how sharp an image appears. Yan et al. (2013) presented using a triangle to fit a gradient of edges and the root triangular parameterization to assess image sharpness. Potentially, certain methods, such as the discrete Fourier transform (DFT), could measure the degree of the blockiness effect. Wang et al. (2000) used DFT after constructing a block effect image and a block-free effect image to quantify the degree of the block influence by analyzing the power spectrum during median smoothing, and this was done to determine which image had a greater impact due to the block.

## 2.6 Conclusion

In general, despite advancements in hyperspectral imaging technology, there is no neurosurgical spectral imaging database for neurosurgeons to utilize as a HS-based reference for diagnostic and surgical cases. This is the case even though there have been developments. In addition, the images that were acquired at KUH do not include a method for evaluating the focus of the brain hyperspectral images. Considering that, a neurosurgical HSI data-architecture has been designed and developed and the designed data-architecture includes a GUI application with a working database that is capable of performing multiple functions, such as storing spectral images, RGB images, annotated images, masked images, and displaying the class tissue and calculating the average spectral reflectance of each tissue class in the spectral image. NR-IQA-based focus assessment method is also tested and experimented on the dataset.





## 3 | Methodology

During the analysis procedure, two sample datasets were employed; one sample dataset covers a band image between 500 nm and 900 nm, and the second sample covers 500 nm to 950 nm. The sharpness level of the spectral band images have been evaluated using various NR-IQA methodologies, and a correlation method has been used to assess the performance of the techniques and to assess the relationship between the wavelengths and the focus of the band images at various wavelengths. A database of the hyperspectral images with its associated class tissues and tumor tissues has been built, and a mean and standard deviation spectral reflectance have been computed in order to prepare a gold standard spectral reflectance of tissue classes and tumor classes on brain images.

### 3.1 Dataset

Raw, unprocessed spectral images of the medical spectral datasets that were utilized in this study had been obtained at the Microsurgery Center of Kuopio's University Hospital. The spectral images were acquired through the utilization of a customized technology. Hardware, software, and the surgical staff in the operating room make up the three primary components in the intraoperative HSI system. The hardware and software are attached to the operation microscope and their combination results in a functional intraoperative HSI system that is managed by a team made up of computer scientists, surgeons, and operating room nurses who have received sufficient expertise in their respective fields (Puustinen et al., 2022).

Using the intraoperative HSI technology described above, a total of 52 microsurgical hyperspectral images from 10 patients have been captured. Optical imaging in neurosurgery usually is divided into three different phases: preoperative, intraoperative, and postoperative image assessment (Puustinen et al., 2022). In conjunction with neuronavigation, preoperative data and the ability of data capturing during brain tumor removal provide surgeons considerable significant assistance. The working group, which included both surgeons and engineers, established a process

for the collecting of HSI data.

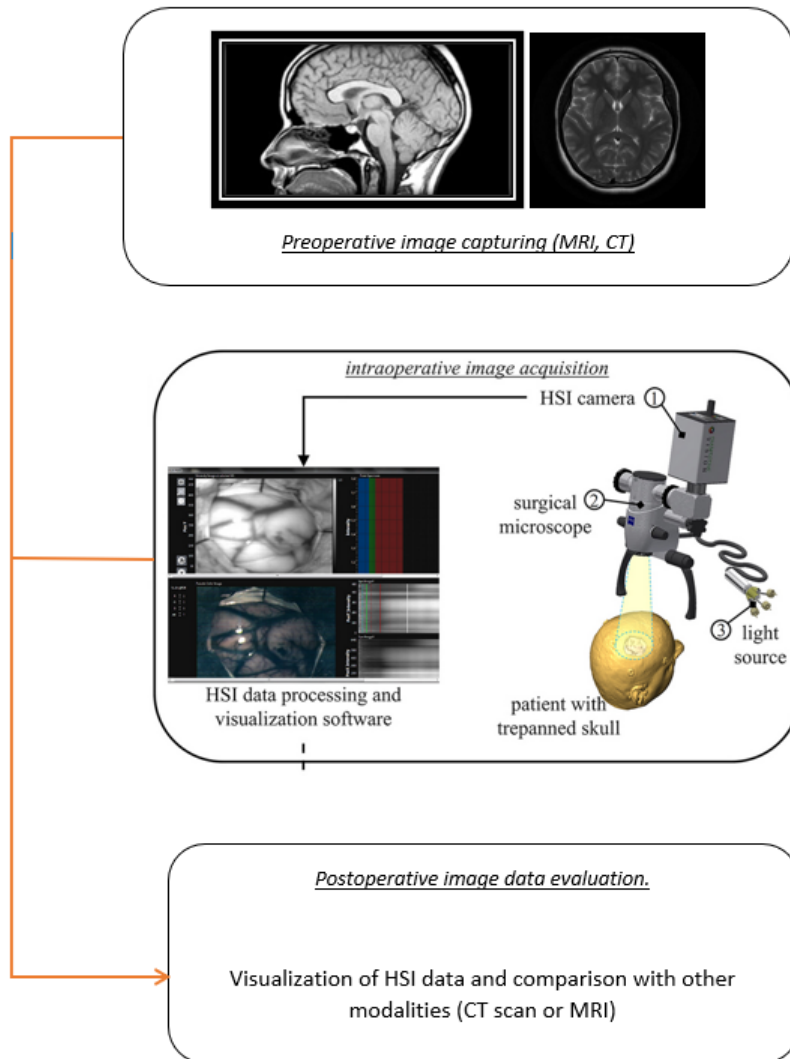
As shown in Figure 3.1, the light source emits light through an optical fiber cable into the surgical microscope's beam path, which is then directed to the cortex via a lens. Following the scanning of trepanning of the skull and the hardware-based raw file pre-processing, the hyperspectral file is then sent to the image processing and visualisation application on the laptop. The program offers details on the location, shape and boundary of the tumor. After performing an intraoperative examination of the spatial and spectral details, the neurosurgeon is then able to proceed with the removal of the brain tumor. During the phase of this workflow referred to as "postoperative image assessment" all of the hyperspectral data that was taken during the "intraoperative" stage are matched and assessed using conventional medical image file processing techniques.

### 3.1.1 Intraoperative microneurosurgical HSI system

The intraoperative hyperspectral imaging system includes a portable hyperspectral camera (Senop HSC-2, Senop Oy, Finland), which is connected to the operation microscope (OPMI-MD, Carl Zeiss Meditec AG, Germany), as well as the microscope's 300 W Xenon light source and a laptop to handle the image collection. The operating neurosurgeon controls the focus, zoom, and light intensity adjustments of the hyperspectral camera, which are connected to the operating microscope. The movement, controls, and balance of the microscope were unrestricted, and the operation microscope and the hyperspectral camera formed an unified single entity that helped to reduce the distraction to the neurosurgeon or the operating room personnel, Figure 3.2 (Puustinen et al., 2022)..

**Hardware:** The HSC-2 HSI camera records spectral data between 500 and 900 nm. The camera captures images in the visible light (VIS) and near-infrared (NIR) wavelengths with a resolution of 1024x1024 pixels using a snapshot-based approach and a CMOS sensor. Maximum image speeds available are 74 fps (12 bit) and 149 fps (10 bit).

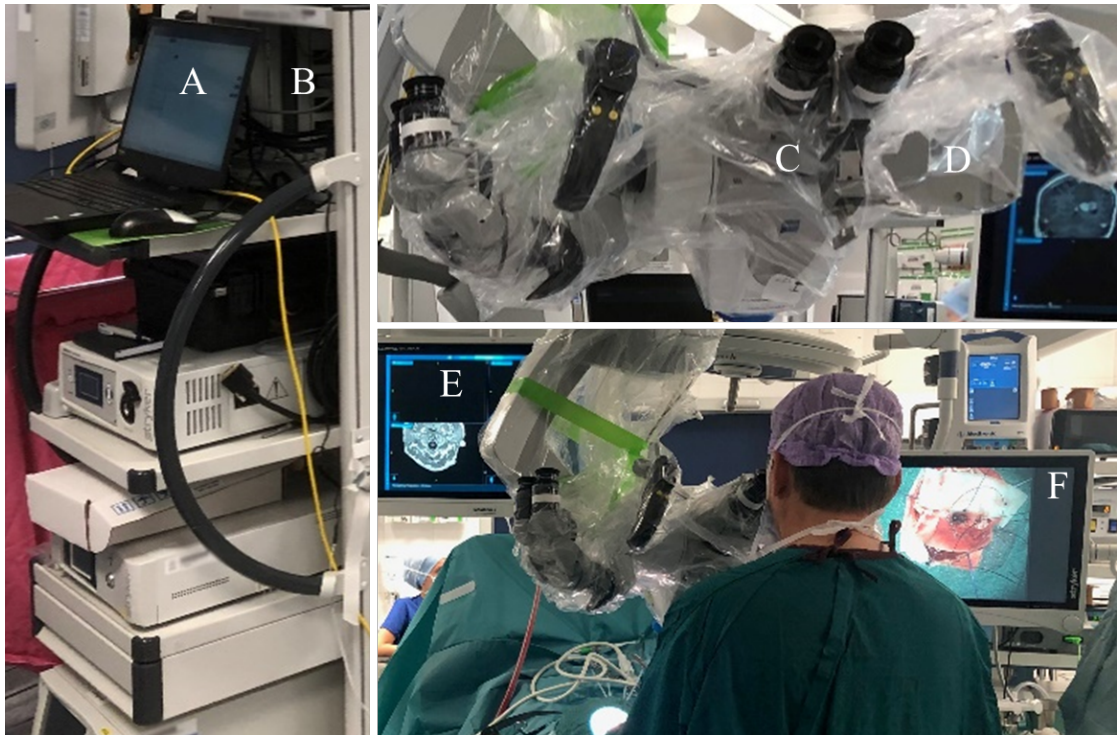
**Software:** The software provided by the camera manufacturer (Senop Oy, Finland) was used to control data acquisition and establish wavelength ranges and exposure periods. Initially, broad wavelength ranges with modest, 3-5 nm increments were recorded to produce an untargeted spectrum of the entire reflectance of different tissues in the operating region.



**Figure 3.1:** Flowchart for the use of HSI systems in neurosurgical applications, including the collecting of hyperspectral data during the removal of brain tumors. The imaging process in neurosurgery may be broken down into three distinct phases: preoperative, intraoperative, and postoperative. The data flow that is being managed between the three phases is shown by the red arrow. hyperspectral imaging camera (1), microscope (surgical) (2), light source (3).

### 3.1.2 Phases of HSI acquisition

**HSI operation preparations:** A dark reference was acquired by covering the lens of the hyperspectral camera. White reference tiles were imaged. The operative surgeon determined the appropriate imaging locations and biopsy areas. The HSI



**Figure 3.2:** *The intraoperative system utilized for hyperspectral data collection. (A) the laptop used to manage the HSI acquisition, (B) the surgical tower, (C) the operation microscope, (D) the HSI camera, (E) the neuronavigation monitor, (F) the monitor displaying the field of view of the operation microscope, and (G) the patient. (Puustinen et al., 2022)*

team created target-specific imaging sequences before the procedure. Preoperatively, the tissue quality and surgical approach were assessed using MRI and brain mapping data.

**Intraoperative HSI data acquisition:** RGB images were acquired from the anatomical reference points corresponding to the respective locations. Throughout the procedure, the imaging times, angles, distances, and illuminations were recorded.

**Postoperative HSI data processing:** Puustinen et al. (2022) mentioned a professional neuropathologist reviewed the tissue samples, categorized the tumors, and contributed digital histological images to the spectral database. The spectral images, which were annotated anatomically alongside the MRI scans and intraoperative RGB videos, were suitably labeled for the improvement of intraoperative HSI data use.

## 3.2 Data pre-processing

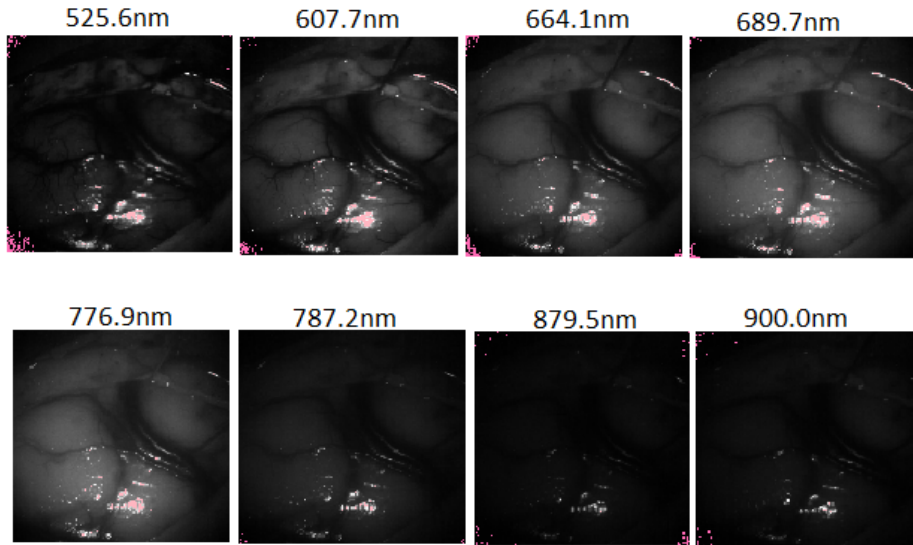
The used hyperspectral brain datasets are obtained at the Microsurgery Center of KUH as raw unprocessed spectral images stored by the Senop-camera in ENVI-format.

The acquired signal for each pixel on spatial location  $(x,y)$  at wavelength  $\lambda$  in a hyperspectral image is of form:

$$s(x, y, \lambda) = I(x, y, \lambda) \times R(x, y, \lambda) \times H(x, y, \lambda) + \eta(x, y, \lambda) \quad (3.1)$$

where  $I(x, y, \lambda)$  represents the illumination on a sample,  $R(x, y, \lambda)$  represents the reflectance of a sample,  $H(x, y, \lambda)$  represents the sensitivity of the spectral camera, and  $\eta(x, y, \lambda)$  represents the noise.

Figure 3.3 illustrates representative bands of the visible-near infrared hyperspectral image of a brain surface acquired by the camera on patient 1. The measured signal is generally low in the IR area and the exposure time is too short in comparison to the illumination intensity (Puustinen et al., 2022).



**Figure 3.3:** The VNIR hyperspectral image's most representative bands (515 nm to 900 nm) from the database of patient-1

The raw images were processed to generate the spectral reflectance images,

which are flat-field corrected (sometimes referred to as white corrected) spectral images. The following equation was applied to the raw images to obtain the spectral reflectance image:

$$R(x, y, \lambda) = \frac{s_s(x, y, \lambda) - s_d(x, y, \lambda)}{s_r(x, y, \lambda) - s_d(x, y, \lambda)} \times R_r(x, y, \lambda) \quad (3.2)$$

where  $s_s(x, y, \lambda)$  is a sample measurement and  $s_d(x, y, \lambda)$  is a dark-current sample captured with no light entering the camera and hence recording only noise,  $s_r(x, y, \lambda)$  is a white reference sample, and  $R_r(x, y, \lambda)$  is the reference sample's (known) reflectance spectrum (Li et al., 2013).

Figure 3.4 shows the reflectance of the dark and white correction methods applied to class of trabecular bone on the raw spectral images acquired from patient 4.

### 3.2.1 Anatomical annotation and labeling

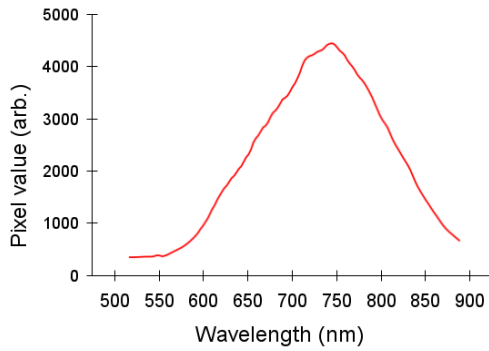
According to Puustinen et al. (2022), the RGB images from the operating microscope were aligned and scaled to match the spectral images. Two neurosurgeons created the anatomical annotations, and a clinical HSI researcher labeled the various tissue regions within the hyperspectral images. The annotation labels were classified as i) healthy tissues, (ii) pathological tissues, (iii) fluorescence, (iv) microsurgical instruments and materials, and (v) irrelevant (such as specular reflections, out-of-focus regions, shadows, and noise), and in the final HSI analysis, the unnecessary regions were excluded.

## 3.3 Neurosurgical HSI system and database architecture

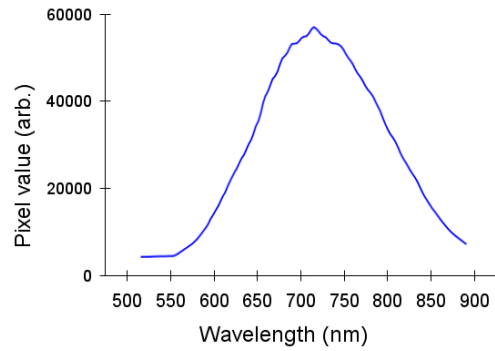
The system and database of the in-vivo hyperspectral human brain image database, which will primarily be used to develop a common brain-image spectral database and to aid neurosurgeons in the identification and delineation of brain tumors by utilizing the non-ionizing and non-invasive hyperspectral imaging modality during surgery has been designed using the Django/Python framework and the PostgreSQL database.

### 3.3.1 System functionality

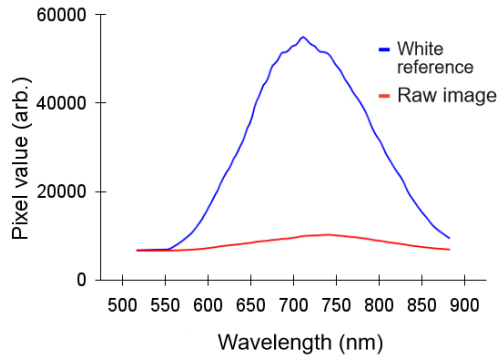
The system will have the fundamental capabilities of displaying a list of thumbnails and the original RGB reconstruction and monochrome image, displaying selected



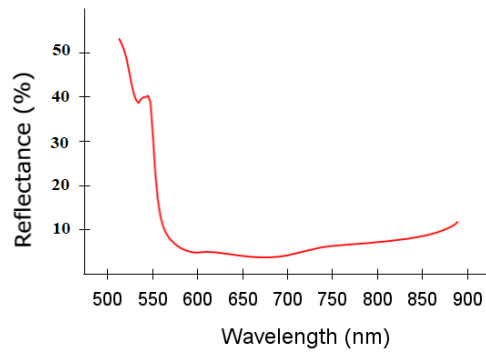
(a) Spectral signature before correction



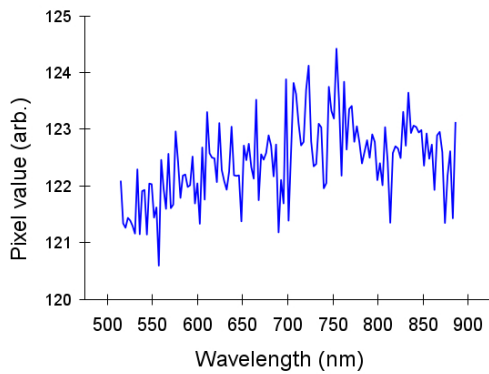
(b) White reference



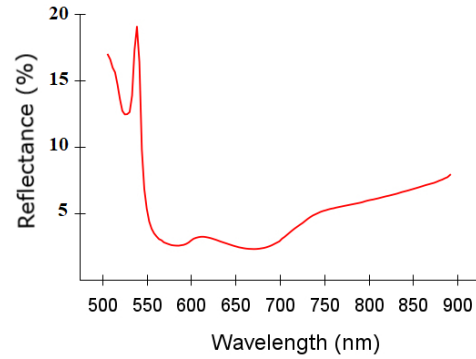
(c) White reference and raw image



(d) White corrected

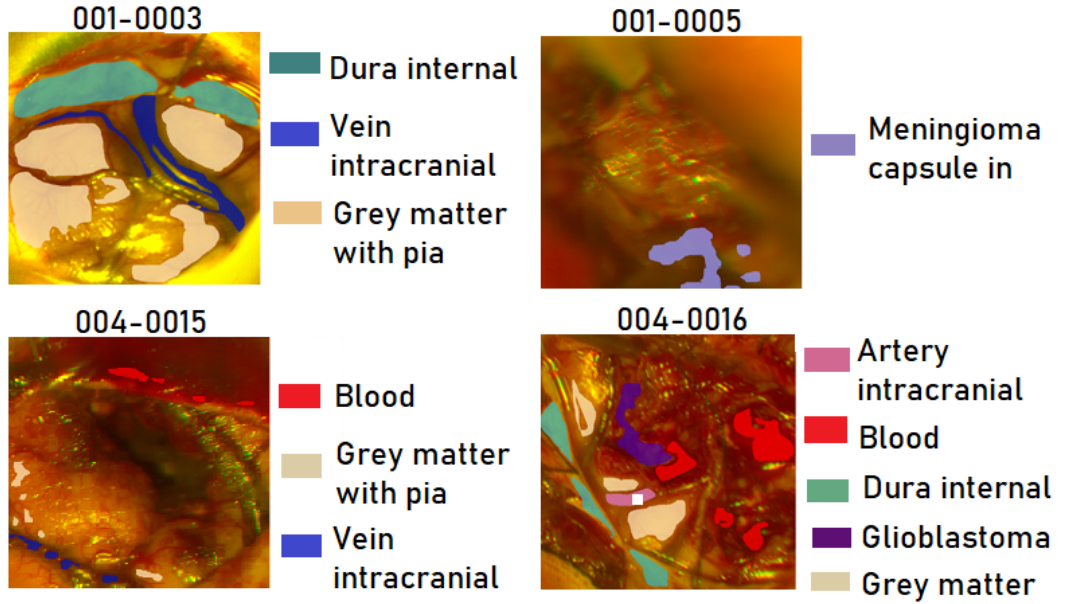


(e) Dark reference



(f) Spectral signature after white and dark correction

**Figure 3.4:** White and dark correction workflow.



**Figure 3.5:** Binary mask representations of the in-vivo hyperspectral human brain image database. The patient and image identification (ID) are represented by the numeric code seen above each image (PatientID-ImageID). The colored regions denote the position of various labeled brain tissue and tumors.

annotation classes and masks as in Figure 3.5, exporting and importing spectral images, and displaying the mean spectral signature for a specified class. In addition, the system will display mean spectral signature (MSS) and normalized spectral signatures for each labeled class, such as cortical vein, as well as a cumulative spectral signature (CSS) of a class from all images in the database.

The mask is represented using a 2d matrix of binary values of zero and one as the mask might be present or absent in HeightxWidth of an area. In order to do that, the number of pixels in a class would be determined by counting the ones from the HxW sum that have the value 1. We utilize a masking function with the formula:

$$f_I(x, y, \lambda) = \begin{cases} i_{x,y,\lambda} & \text{if } m_{x,y} = 1 \\ 0 & \text{otherwise} \end{cases} \quad i_{x,y} \in \mathbf{I}_{\text{image}}^{W \times H \times \Lambda}. \quad (3.3)$$

Where  $f_I$  is the masking function, H is the height, W is the width, m represents a pixel in HxW, i represent the presence of a mask in HxW, and I represents a pixel in the image.

We count the pixels inside the HxW to determine how many pixels are avail-



able in a mask. To count number of pixels from a mask image, we use:

$$NP_{\text{image,class}} = \sum_{x=1}^W \sum_{y=1}^H m_{x,y} = 1 \quad m_{x,y} \in \mathbf{M}_{\text{image,class}}^{W \times H} \quad (3.4)$$

Where NP is the number of pixels in the class, M is the vector of the masked class, and m is the masked class.

The spectrum will be obtained from a range of band numbers since we are computing the mean spectrum in a certain range of bands.

**MSS** is a vector of  $n$  bands

$$MSS_{\lambda}^{\text{image,class}} \in \mathbf{MSS}^{\Lambda} \in \mathfrak{R}^n$$

Where  $\Lambda$  is the potential range of wavelengths in the acquired image and  $\mathfrak{R}^n$  is real valued  $n$ -element vector.

To calculate the mean spectrum for a class, we use:

$$MSS_{\lambda}^{\text{image,class}} = \frac{1}{NP_{\text{image,class}}} \sum_{x=1}^W \sum_{y=1}^H f_I(x, y, \lambda), \quad (3.5)$$

When an image is added to the database, the cumulative spectral signature (CSS) will be computed by:

$$CSS = \frac{(\mu * NP + \mu_a * NP_a)}{(NP + NP_a)} \quad (3.6)$$

and when an image is deleted from the database, the cumulative spectral signature (CSS) will be computed by:

$$CSS = \frac{(\mu * NP - \mu_a * NP_a)}{(NP - NP_a)} \quad (3.7)$$

where  $\mu$  is the class pixel mean value prior to addition/deletion, NP is the class number of pixels prior to addition/deletion,  $\mu_a$  is the pixel mean value of class in the image to be added/deleted and  $NP_a$  is the number of pixel of the class in the image to be added/deleted.

## 3.4 Blur-specific quality assessment of spectral band images

To achieve an accurate representation of the various tissue and tumor reflectances during microsurgery, having sharp spectral band images is essential. Therefore,

the image quality assessment (IQA) approach has become an essential procedural technique that is used to evaluate the sharpness of the spectral images that were obtained at the hospital before utilizing the spectral information as a reference in the intraoperative treatment or before adding the spectral image to the developed HSI database as gold standard.

The spectral band dataset that are acquired at KUH are used during the sharpness assessment, and to produce a dataset with different bluriness level for focus analysis, the band images were blurred using a gaussian filter technique with varying sigma values, as shown in Figure 3.6. When using the Gaussian blur algorithm, the pixels that are closer to the kernel's center are considered more important than the pixels that are further away from the center. This averaging is carried out on a channel-by-channel level, and the values of the channel that are averaged end up becoming the new value for the pixel of an image that has been filtered. The purpose of the sigma parameter with in Gaussian filter is to regulate the variance that occurs around the mean value. Thus, as sigma increases, variance around the mean increases, and as sigma decreases, variance around the mean decreases.

### 3.4.1 NR-IQA Algorithms

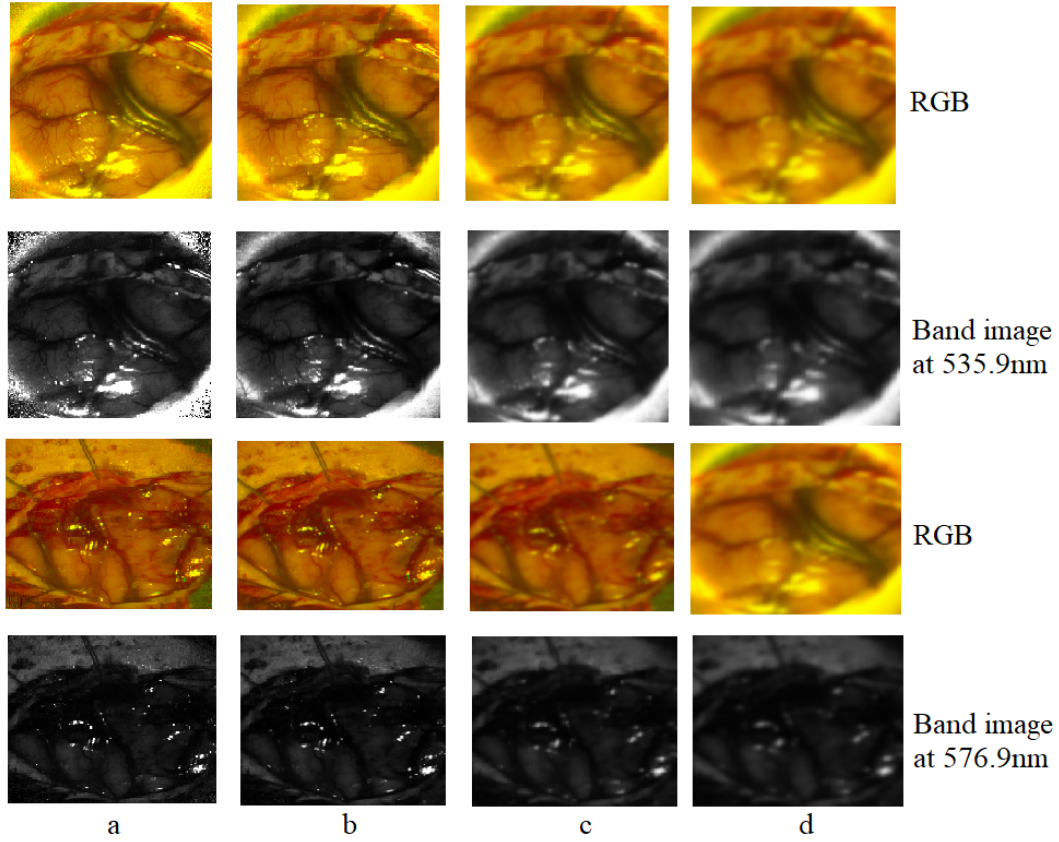
In accordance with the categorization that (Li and Jiang, 2019) provided for NR-IQA approaches that were used in RGB images, the NR-IQA methodologies can be subdivided into two approaches: learning-free and learning-based approach. As part of the work for this thesis, we are concentrating on studying the focus of the band images at different wavelengths using a transform-free and handcrafted feature-based (natural scene statistics) approaches as represented in Figure 3.7.

#### 3.4.1.1 Perceptual Sharpness Index

An edge-based method named the Perceptual Sharpness Index (PSI) was developed after statistical analysis (Feichtenhofer et al., 2013). The approach's first step is to choose the most crucial edges in the region using an adaptive edge selection algorithm. In the second step, edge widths of the chosen edges are estimated using diagonal gradient measurements. Third, slopes of the edge are used to remove edge widths higher than the just noticeable blur (JNB) threshold. Finally, a block-wise combination of the previous three processes yields the local sharpness map.

*Steps:*

- i ) *Adaptive Edge Selection.*



**Figure 3.6:** Raw RGB and band images with their corresponding blurred images a) RGB and band images acquired at KUH b) RGB and band images with gaussian blur ( $\sigma = 1$ ) c) RGB and band images with gaussian blur ( $\sigma = 3$ ) d) RGB and band images with gaussian blur ( $\sigma = 4$ ). Rows 1 and 2 belong to patient 1 in the database, whereas rows 3 and 4 belong to patient 4 in the database.

The initial phase of the method is to create an edge map, which represents the image's most important features. To achieve this, a Sobel filter (vertical and horizontal) is employed to the image's luminance channel, followed by thresholding and thinning method. The Sobel filter outputs are squared pointwise and added together to give an estimate of the image squared gradient  $G$ , this gradient  $G$  is then thresholded using an adaptive threshold.

$$T = \alpha \cdot \overline{G}, \quad (3.8)$$

where  $\overline{G}$  represents the average value of  $G$ , and  $\alpha$  is a scaling factor that is determined by an experimental investigation of the effect of a parameter on the



**Figure 3.7:** A comprehensive categorization of blur-specific, no-reference image quality evaluation techniques, including learning-free and learning-based techniques.

variable. The adaptive threshold 3.8 focuses on the image’s most significant edges by calculating the average gradient energy of the image’s edges. In the Human Visual System (HVS), information is encoded in measures of contrast rather than absolute intensities, therefore this focus on relatively high contrasts conforms to human perception (Hubel and Wiesel, 1998). To create an edge map, a nonmaximum suppression is applied to the edge gradients after the thresholding step.

ii ) *Measurement of Edge Width.*

The widths of the relevant edges are measured pixel-by-pixel along the gradient of the edge. The angle between the gradient direction and the tracing direction is represented by  $\Delta\phi(\mathbf{x})$ , where image gradient components  $I_x$  and  $I_y$  are calculated using finite differences. Consequently, at each edge  $\mathbf{x}$  with an estimated vertical gradient direction  $\Delta\phi(\mathbf{x}) < \Delta\phi_{max}$ , the edge width is determined by

$$w(\mathbf{x}) = \frac{w_{up}(\mathbf{x}) + w_{down}(\mathbf{x})}{\cos(\Delta\phi(\mathbf{x}))}, \quad (3.9)$$

Where  $w_{up}\mathbf{x}$  is the distance from the identified edge pixel  $\mathbf{x}$  to the local maximum  $I_{max}\mathbf{x}$ , and  $w_{down}\mathbf{x}$  is the distance from the detected edge pixel to the luminance pixels of the traced local minimum  $I_{min}\mathbf{x}$ .

iii ) *Modelling Human Acutance Perception.*

Receptive retinal cells are considerably highly sensitive to contrast along a

border than to the total light level (Hubel and Wiesel, 1998). Thus, the human vision system is more responsive towards signal contrast than it does to absolute local signal intensity. Since sharper edges are associated with higher contrast, edge slopes have been used as a metric and the slope is calculated as follows:

$$m(\mathbf{x}) = \frac{I_{\max}(\mathbf{x}) - I_{\min}(\mathbf{x})}{w(\mathbf{x})}, \quad (3.10)$$

Implying  $[0,1]$  is the luminance range. In order to evaluate high contrast edges relatively sharper, the estimated edge width is reduced according to the edge slope.

$$w_{\text{PSI}}(\mathbf{x}) = \begin{cases} w(\mathbf{x}) - m(\mathbf{x}), & \text{if } w(\mathbf{x}) \geq w_{\text{JNB}} \\ w(\mathbf{x}), & \text{otherwise} \end{cases} \quad (3.11)$$

Only widths above a minimal width  $w_{\text{JNB}}$  are decreased to signify the just-noticeable difference (JNB) as perceived by the human visual system. The JNB width is the minimum threshold of observed blurriness around an edge, that relies on the local contrast in the surrounding of the edge.

iv ) *Estimation of Local Sharpness.*

Image blocks of 8x8 pixels are used to calculate local sharpness values. Because of the quantization phase of one pixel in the process of measuring edge width, narrow edges may cause a significant amount of quantization error. It requires at least one estimate from the block's broad edges, or two or more estimate from the block's narrow edges. This equates to a minimum amount of 2 for all widths measured within a block. The local sharpness values are then calculated as reciprocal of the averaged  $w_{\text{PSI}\mathbf{x}}$  of all measures in a local block.

v ) *Estimation of Global Sharpness.*

A percentile pooling of local sharpness estimates is used to compute PSI in images with substantial depth-of-field effects in order to adjust to human sharpness perception. The highest percentile average of local sharpness values throughout the image is used in the computation. The idea behind percentile pooling is that the sharpest parts of an image have a big effect on how sharp it looks to the human naked eye.

### 3.4.1.2 Discrete Tchebichef Moments

According to Li et al. (2015b), an edge free method of maximum local variation (MLV) for every pixel is defined as the highest intensity variation of a pixel in

comparison to its 8 neighboring pixels based on the discrete Tehebichef moments (DTM). Due to the fact that the HVS responds best to higher variations in intensity, higher variations of intensities in the pixels serve as optimal sharpness measurement. Finally, to quantify sharpness, the weighted MLV distribution's standard deviation is used.

### 3.4.1.3 Local phase coherence (LPC)

Hassen et al. (2013) suggested a blur-specific NR-IQA methodology based on the Local phase coherence-sharpness index (LPC-SI). They assessed their proposed approach on four relating publicly available image datasets, which shows competitive performance when compared to existing state-of-the-art techniques.

An image must pass over three-scale eight-orientation log-Gabor filters before the score can be measured. The strength of the LPC is then estimated at one spatial location and one orientation, and then at all spatial location. LPC, on the other hand, does not use block-based processing like other algorithms.

### 3.4.1.4 Difference of differences in grayscale measurements of a median-filtered image

Kumar et al. (2012) proposed an approach for measuring the sharpness of edges that, instead of measuring edge-width, measures the shifts in luminance (grayscale) values observed at an edge. The approach could be used to estimate image sharpness when images are blurred owing to camera motion (or handshake), defocus, or problems from imaging system.

Sharpness estimate is done individually in the x and y dimensions. To rapidly detect edges, the image would be initially smoothed with a one dimension filter ( $[\frac{1}{2} \ 0 \ \frac{-1}{2}]$ ) in x or y dimension. The region of absolute values larger than a threshold is picked to identify likely edge pixels. The normalized estimate for each edge-pixel is determined, and the pixel is categorized as sharp if it exceeds a defined threshold target.

The sharpness  $S_x(m, n)$  in the x-dimension for a pixel situated at  $i, j$  in an image is calculated as follows:

$$S_x(m, n) = \frac{\sum_{m-w \leq k \leq m+w} |\Delta DoM_x(k, n)|}{\sum_{m-w \leq k \leq m+w} |I(k, n) - I(k-1, n)|} \quad (3.12)$$

Where  $w$  is the width of the noticeable blur,  $\Delta$  is the difference of differences in intensity of a median-filtered image as a measure of edge sharpness, and  $I(k, n)$  is

the value of a pixel in the image situated at  $(k, n)$ .

The ratio has a high value in sharp areas and a low value in blurred areas. In the y-direction, a similar calculation is performed to yield  $S_x(m, n)$ . The sharpness estimations for each edge-pixel must be merged to determine the sharpness of the an image. Sharpness in one dimension (x or y) for an area or the whole image is calculated as follows:

$$H_x = \frac{\text{sharpPixels}_x}{\text{edgePixels}_x} \quad (3.13)$$

$$H_y = \frac{\text{sharpPixels}_y}{\text{edgePixels}_y} \quad (3.14)$$

Finally, using a Frobenius-norm, the sharpness with in x and y dimensions is merged to get the sharpness ( $S_n$ ) of the band image:

$$S_n = \sqrt{S_x^2 + S_y^2} \quad (3.15)$$

When all edge-pixels in x and y directions are identified as sharp,  $S_n$  could reach its maximum value of 2.

### 3.4.1.5 Blind Image Blur quality Evaluator (BIBE)

Images are supposed to have particular mathematical distribution that may be changed by the presence of distortions. Consequently, the quality of band images could be evaluated by analyzing at the deviations from the statistical distributions, which can be done by simulating the statistical parameters of image coefficients. (Wang et al., 2015) introduced a NR-IQA blur-specific technique BIBE, which is based on the natural scene statistics of gradient distribution as represented in Figure 3.8. First, the gradient map is created by applying the vertical and horizontal filters on the blurred image. The histograms' gradient-related distributions are then simulated using a generalized Gaussian distribution (GGD) or an asymmetric GGD. The extreme learning machine is then applied to the NSS features (model parameters) to estimate the band image quality.

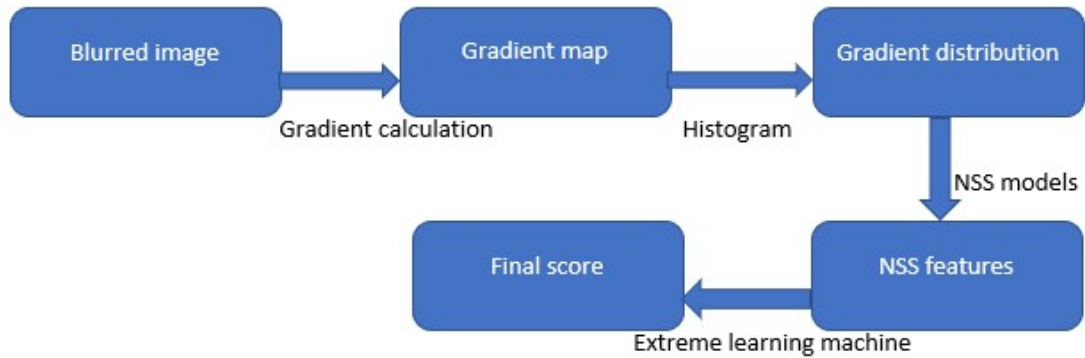


Figure 3.8: Flowchart of NSS-based BIBE method

### 3.4.2 Support Vector Machine (SVM) for sharpness classification of band image

In machine learning, Support Vector Machine (SVM) can be used for both regression and classification tasks, but it is most commonly used for classification.

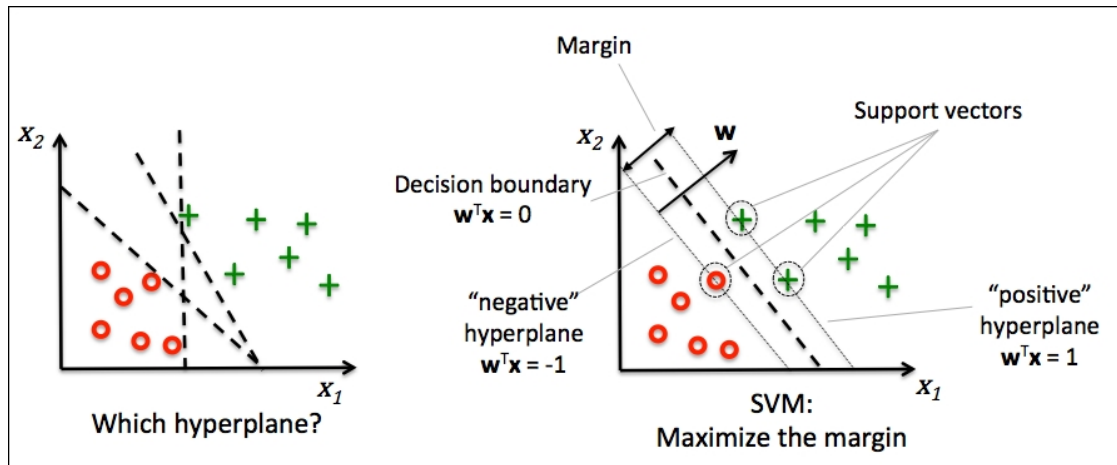


Figure 3.9: Hyperplanes in SVM

The goal of the SVM algorithm, as shown in Figure 3.9, is to search a hyperplane in an N-dimensional space (N being the number of features) which distinctly classifies the data points.

There are numerous hyperplanes that could be used to distinguish between the two classes of data points. Our objective is to determine the plane with greatest margin, or lengthy distance between the sample points from the two different classes.



Increasing the margin distance provides assurance that can allow future data points to be categorized more accurately in to the right class. For classifying the data points, the hyperplanes act as decision boundaries. The size of the hyperplane is dependent on the number of features; for example, if there are two input features, the hyperplane will be a line, and if there are three, it will be a two-dimensional plane.

There are two types of SVM algorithms for classification: Soft Margin and Hard Margin:

**Soft Margin** we add a degree of tolerance, allowing the model to voluntarily misclassify only few data points if it means identifying a hyperplane that can generalize better to unseen data.

**Hard Margin** attempts to find the best hyperplane while not tolerating any type of misclassification

Support vectors are data points that are close to the hyperplane and have an effect on its position and orientation. Using these support vectors, we maximize the classifier's margin. If the support vectors are removed, the hyperplane will shift in position, and these are the points that aid in the development of the SVM model.

SVM uses three parameters: kernel, C, and gamma. Kernel can have various "values" such as linear and poly. C governs the tradeoff in between smooth decision boundary and correctly classifying the points. Gamma reflects the amount of influence that a single training instance could have. The greater the gamma value, the closer other instances being affected. In general, the selection of these parameters has an impact on the SVM algorithm's performance.



## 4 | Results

### 4.1 Database architecture

As the neurosurgical HSI navigation currently lacks coherent data collection conventions and standardized tissue classes in a databases, this thesis work has designed a data architecture that can be used to control the data flow of the neurosurgical spectral images. Figure 4.1 illustrates the data architecture design of the database.

The database (Appendix A.1, A.3) contains 52 hyperspectral images obtained during microneurosurgical operations performed at Kuopio University Hospital (KUH). Device and imaging information are among the information found in the designed database with the neurosurgical database. The following list illustrates some of the database's features.

#### 4.1.1 Imaging case data classes

The designed data architecture and database would have different class types that would appear as tables with the appropriate relationship between each class. The items listed below are some of the classes obtained prior to the postprocessing stage of the acquired data.

**Patient ID** a unique identifier for each patient in the system.

**Diagnosis** a textual description of the diagnosis.

**Image or image series ID** a unique identifier identifying an image or image series related to a patient.

**Optic imaging system name** the light and special photon properties to acquire images of tissues, cells, and tumors, allowing for minimally or non-invasive processes of looking inside the body.

**HSI camera** the hyperspectral camera used in the image acquisition.

## Chapter 4 | RESULTS

**HSI Software name and version:** Software used to acquire the hyperspectral image.

**Acquisition type** the type of image acquisition technique used.

**Timestamp (clock/day/month/year)** time when the image acquisition happened.

**Data size** The size of the hyperspectral image.

**Resolution (height x width)** number of pixels represented per image inch.

**Bandpass range** the range of wavelength frequencies.

**Frames (n)** number of frames.

**Imaging magnification** the size of the object that created from the microscopic image in relation to its original size.

**Imaging focal length** the distance when the object is in focus in between lens and the image sensor.

In addition to the database classes listed above, additional classes will be obtained during the data architecture's post-processing of the data. Following the postprocessing stages, the following classes are obtained:

**Label library name and version** text description of the library name and its version.

**Reference RGB** RGB image ID (from e.g., microscope).

**Tissue classes** number of labels in library.

**Class features** number of features for each class.

**Annotation rate** % of area annotated.

**Description rate** % of classes featured.

**Notes** Description of the tissue classes and tumors.

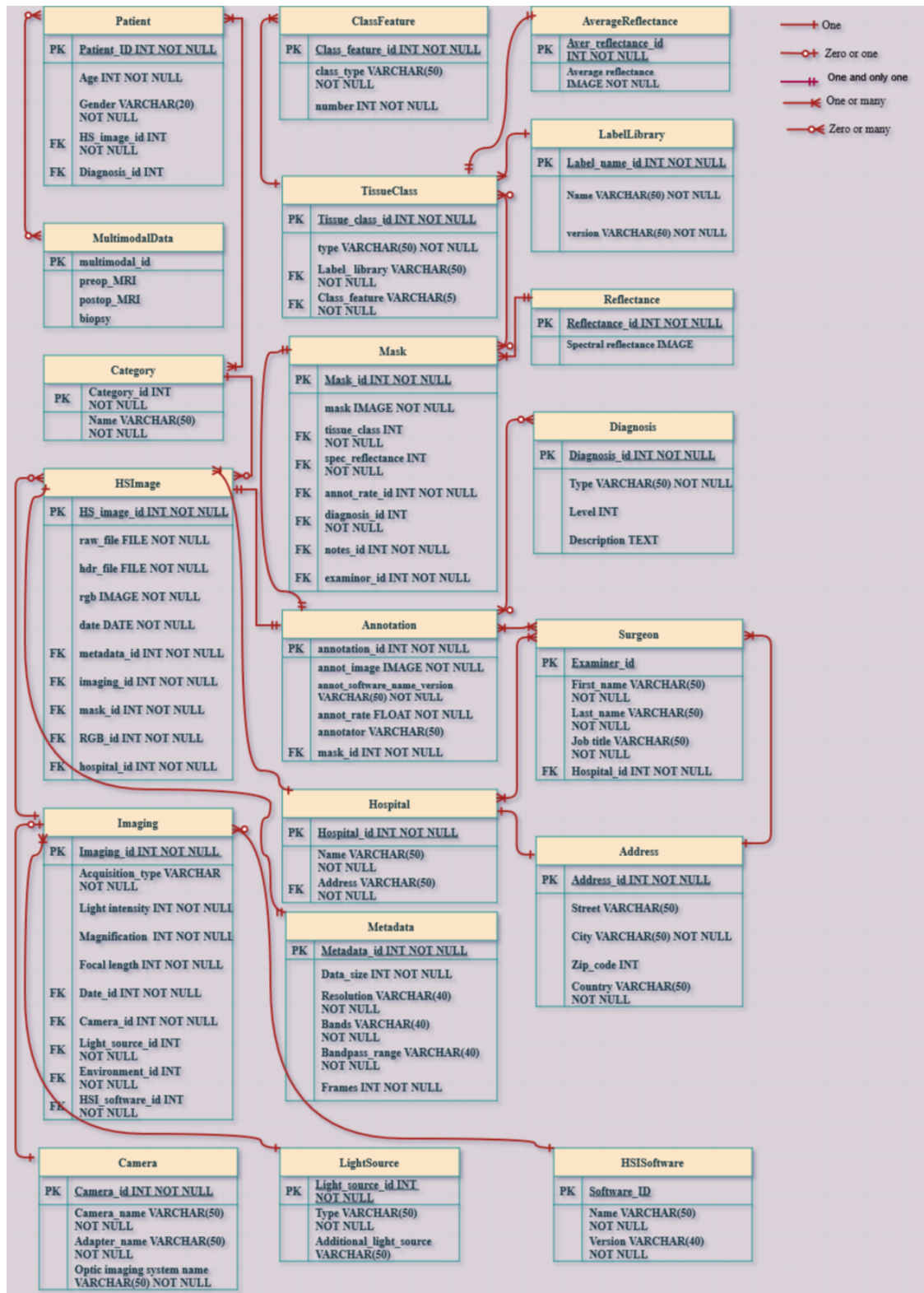
## 4.1.2 Tissue classes and class features

Most of the spectral images in the database have the following tissue classes and subclasses: dura (periosteal, meningeal), bone (compact, trabecula), parenchyma (grey matter, white matter, monitored tract), artery (intracranial, extracranial), vein (intracranial, extracranial), cranial nerve, ependyma, pathology (glioma, meningioma, aneurysm), blood (arterial, venous, mixed) and synthetic. Each tissue class in the database shares one or more of the following class features: subarachnoid intact, bare intact, manipulated, cauterized, fluorescent and removal.

Figure 4.1 illustrates the designed data architecture for the microneurosurgical HSI database. A relational database is created, which is a collection of data that arranges data points into tables with rows and columns and established relationships for easy access. Information about related objects is kept in a relational database's data tables. Each column has the data attributes, and each row comprises a record with a unique identifier, or key. Each feature is given a value in each record, making it easy to identify the relationships between different data points. According to the object-oriented paradigm, a table of a relational database would be represented as a class, columns as its attributes, and rows as its instances. The object-relational mappers for relational database management systems typically offer an SQL-based interface, and the classes that model tables in Django are known as models, and the class attributes that model columns are known as fields. The mapper also abstracts common relations into classes that can be used as field types in models to connect to other models.

The database will include many relations and relationships between the tables. The database's common tables are 'Patient,' which shows patient age, 'ClassFeature' which shows the number of features in each class, 'TissueClass' which contains the class of a specific tissue, 'Mask' which contains the masked image, 'HSImage', which includes the image's raw and HDR files, 'Imaging,' which includes the information about light intensity, focal length, and magnification, and 'Metadata,' which includes information about data size, resolution, bands, and frames.

Each instance of a model is differentiated by a primary key (PK) which is a unique identifier. An instance of one model could define a foreign key (FK) that refers to the primary key of another instance of the model, thereby establishing a relationship between the models. For instance, the "Patient" model has a one-to-many relationship with the "HyperspectralImage" model. This indicates that a single instance of the "Patient"-model can be associated with multiple instances of the "HyperspectralImage" model (i.e., the system allows multiple hyperspectral images per patient). For the relation to be implemented, the "HyperspectralImage"

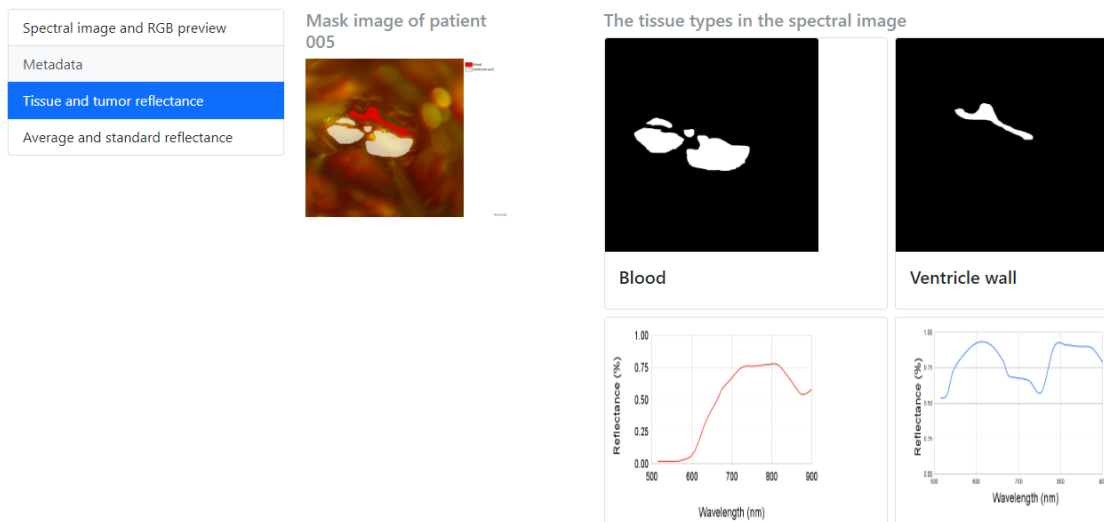


40 **Figure 4.1:** Designed data architecture for the microneurosurgical HSI database, illustrating data model relationships. Crow's foot notation is used to represent one-to-one, one-to-many, and many-to-many relationships between models.

model should define a foreign key to the "Patient" model.

## 4.2 System architecture and functionality

The database and system in general will have various basic and advanced functionalities that can be used to assist surgeons in delineating healthy tissues and tumors during a brain surgery using spectral technology cameras, multimodal images such as MRI, and spectral reflectance values of different tissues that were stored in the database can be used as gold standard during the surgery. To demonstrate the technical methodology the images and results used in this report are from patient ID #0003 in the database. Figure 4.2 shows an example of the GUI web page interface that can be used to search information from the database using the patient ID, spectral image ID, class tissue, and/or tumor category. The Appendix A section also contains additional images from the GUI and database.



**Figure 4.2:** *Reflectance properties of tissue and tumor classes from the GUI.*

The designed system will have the following basic functionalities:

1. To display list of thumbnail RGB reconstruction or monochrome image
2. To display selected annotation classes and masks
3. To open, export and import a spectral image

4. To display averaged spectral signature for selected labeled class (e.g. artery)

The designed system will also have the following advanced functionalities:

1. To display cumulative spectral signature of a class from all database images
2. To display averaged, normalized and outliers spectral signature for each labeled class e.g. cortical Vein

where,

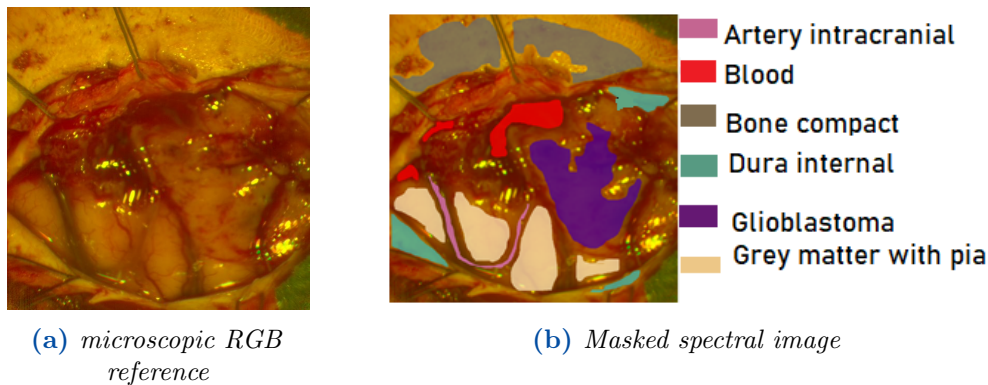
- Averaged = average from all labeled areas of a single class in an image
- Normalized = Set the range of data's features to between 0 and 1.
- Outliers = an observation that deviates abnormally from other reflectance values in the given database in terms of spectral signature.

Using the Django framework, a full-stack web application has been developed. The framework integrates a number of technical features into a unified system, making prototyping and experimentation easier. The framework supports input logic, business logic, and user interface logic (UI) via a model-view-controller architecture. The model is a web application component that serve as a gateway between the graphical interface and the database, as well as the entity that enacts the logic for the application's data domain. In the architecture of the framework, the view component contains the UI logic and provides the web-based graphical user interface (GUI). Finally, the controller is responsible for handling user interaction and choosing a view based on a model.

Figure 4.3 shows one of the HSI mask with tissue and tumor areas that is stored in the database. Tumors, materials, and tissue classes such as artery, vein, bone, and blood that appear in the surgical scene were labeled in these images. The sample of mean and standard deviation of a particular brain tissue and tumor provided in the DB across all patients, distinguishing between the various brain tissue and type of tumor is shown in Figure 4.4 and Figure 4.5.

Figure 4.4 illustrates the reflectance of various class tissues and a glioblastoma tumor observed in the database. The spectral signature of those classe tissue and tumor can be computed, and it will be possible to compare their reflectance result with the gold standard mean spectral reflectance that was originally computed from different similar tissue classes, and surgeons can easily identify the class of a specific tissue based on its reflectance properties during an intraoperative neurosurgical operation.

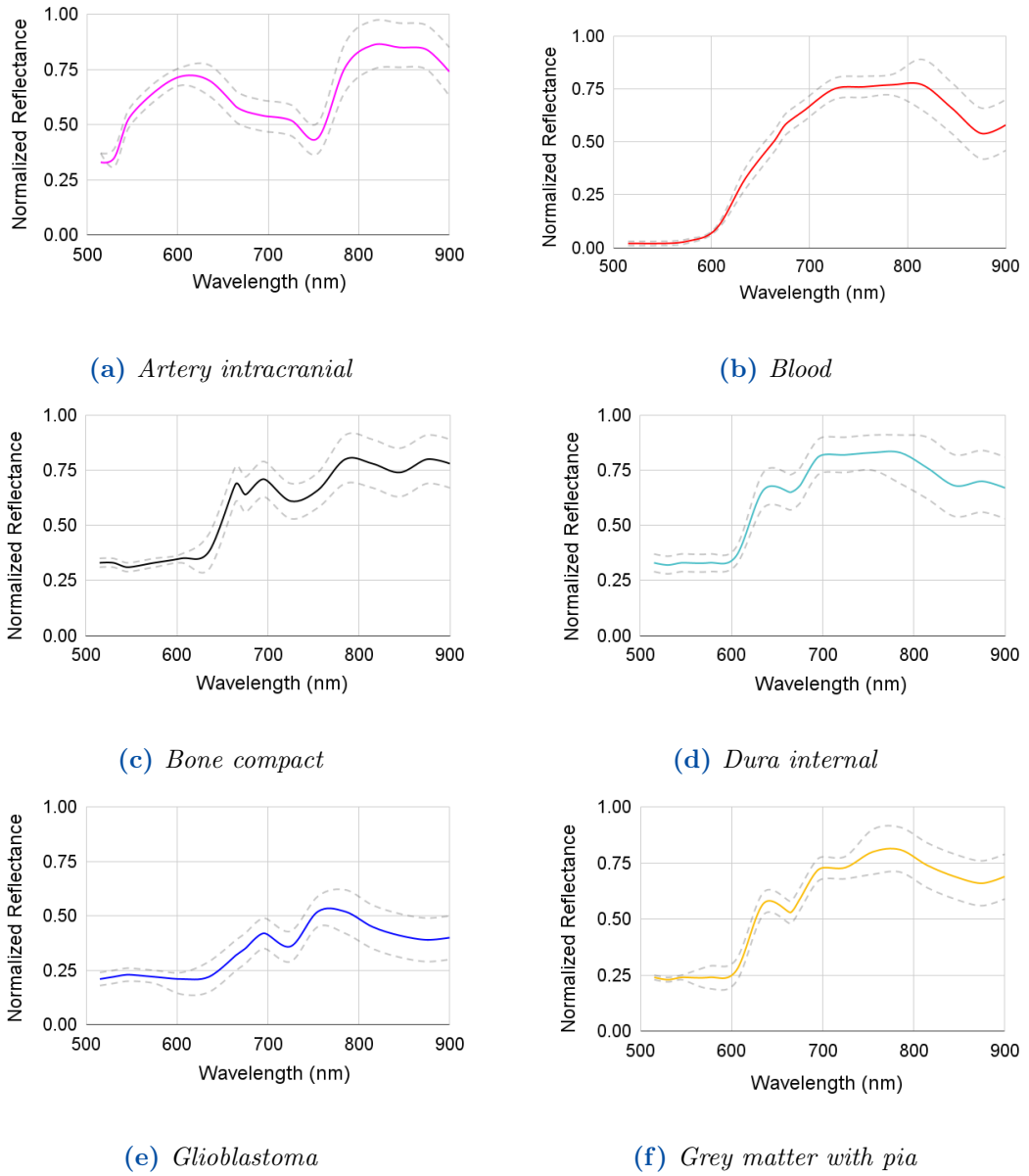




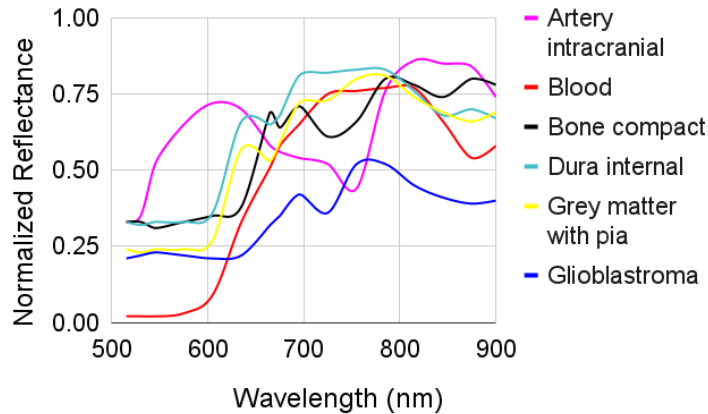
**Figure 4.3:** a) RGB reference image of an operation microscope b) The associated HSI mask of patient ID 0003 with labeled healthy tissue and tumor areas. Anatomical annotations provide localizing information, while tissue labels delineate the relevant features for the HSI analysis.

The standard deviation measures how distributed the wavelength reflectance is in comparison to the average. A low deviation indicates that wavelength reflectance is heavily focused around the average, whereas a high deviation indicates that wavelength reflectance is more dispersed. A high deviation implies that wavelength reflectance points are above the average. In Figure 4.4, the dashed lines above and below the average reflectance indicate more spread out reflectances and thus a higher standard deviation, whereas the dashed lines closer to the average reflectance indicate more clustered around the average and thus a lower standard deviation.

Figure 4.5 demonstrates the average reflectance properties of all images in the database with similar tissue class type. For example, as shown in Figure 4.5, 'dura internal' and 'bone compact' have similar spectral signature responses in the 500 nm to 650 nm range, but from 650 nm to 900 nm we can easily distinguish those two classes based on their reflectance results. Similarly, 'gray matter with pia' and 'glioblastoma' show similar reflectance between 500 nm to 600 nm, but after 600 nm to 900 nm the two different classes respond with different spectral reflectance values, which can be used to distinguish between the different classes of tissues. In general, with the help of other modality images, the average reflectances obtained from multiple gold standard spectral images at different wavelength points can be used to distinguish the tumor from healthy tissues during an in-vivo neurosurgical operation.



**Figure 4.4:** The mean and standard deviation spectral signatures of different tissue and tumor type across all patients in the database between 500 nm to 900 nm wavelength range. Using feature scaling, the reflectance values are normalized to between 0 and 1. (a) Artery intracranial; (b) Blood; (c) Bone compact; (d) Dura internal; (e) Glioblastoma; (f) Grey matter with pia.



**Figure 4.5:** Mean spectral reflectance for different class tissues from the gold standard spectral images in the database.

## 4.3 Blur-specific quality assessment of the hyperspectral image bands

When each of the previously stated NR-IQA algorithms was applied to the hyperspectral image database, an objective value was calculated. Following that, two performance measurements are computed to assess the IQA approaches performance: 1) Spearman's rank-order correlation coefficient (SRCC), which is used to assess the performance of the NR-IQA technique, and the degree of association using monotonic function between the focus of wavelengths within different spectral images; 2) Pearson's linear correlation coefficient (PLCC) that evaluates the performance of the NR-IQA technique and the linear correlation between the sharpness score of wavelengths within different spectral images. To achieve a better NR-IQA technique, the SRCC and PLCC values are expected to be close to 1.

The sample data has been split into two separate parts, with sample 1 containing band images that range from 515 nm to 700 nm (95 spectral images each contains 21 band images on average) and sample 2 containing band images that cover 700 nm to 950 nm (95 spectral images each contains 26 band images on average). For a better understanding and tracking of the algorithm performance at various wavelengths, the two samples have been evaluated separately.

Correlation techniques have been computed using objective NR-IQA scores and subjective scores to measure how each NR-IQA method performs in the assessment

of the focus of the spectral band images, and to measure the strength of the relationship between the focus of the wavelength within different spectral images. A correlation close to -1 or +1 indicates a good NR-IQA technique and/or a strong relationship in focus level between the band images at the same wavelength, while a low correlation (close to 0) result represents a weak NR-IQA technique and a weak association between the focus level of band images within different spectral images.

Table 4.1 show the results obtained in the HS database using the previously described methods for samples 1 and 2. The results show a performance comparison of the acquired band images and the blurred images of both samples. Some methods produced a low correlation result with SRCC and PLCC values less than 0.7, while others produced a good correlation with SRCC and PLCC values greater than 0.8. In both samples, PSI and MLV produced a better correlation. Additionally, computational time is a good indicator of algorithm performance, and the execution times of each algorithm have been recorded with the intention of using them as a predictor of algorithm performance.

The NR-IQA algorithms, which were previously evaluated on other RGB images, performed well on spectral band images as well. PSI performed better than the other techniques in sample 1 with 0.92 SRCC, and MLV performed better in sample 2 with 0.87 SRCC. All techniques had an execution time of less than 2.2 seconds for the specified number of images in each sample, with PSI having the better execution time of 0.8s in sample 1 and 0.82s in sample 2.

**Table 4.1:** Correlation results with different approaches. Bold scores indicate a better assessment outcome when compared to the other approaches.

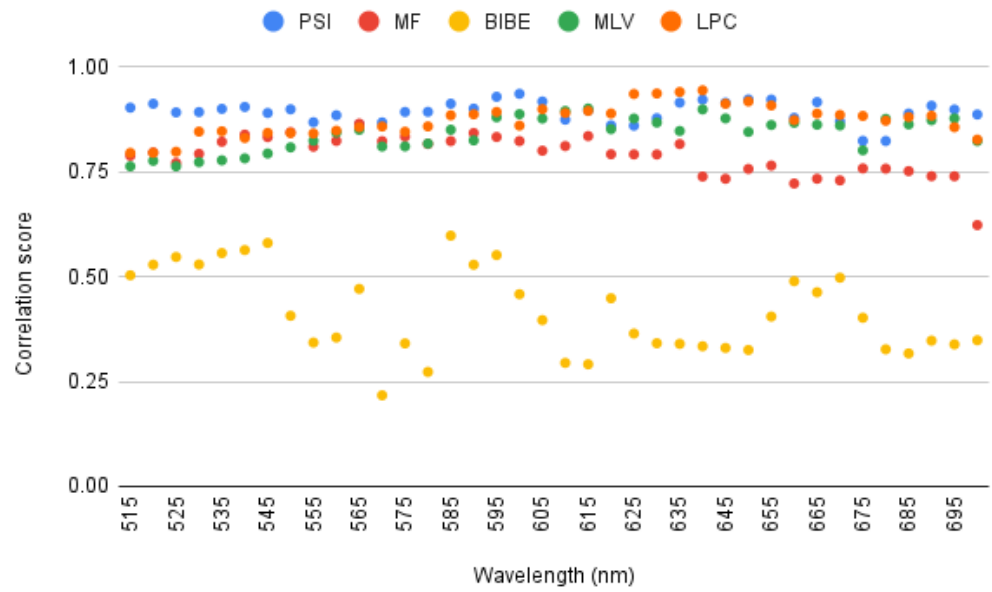
Method	515nm-700nm			700nm-950nm		
	SRCC	PLCC	Time(s)	SRCC	PLCC	Time(s)
PSI	<b>0.92</b>	0.88	0.8	0.86	0.88	0.82
MF	0.69	0.74	1.33	0.50	0.54	1.31
BIBE	0.51	0.40	2.2	0.49	0.38	2.2
LPC	0.86	0.84	1.54	0.81	0.79	1.53
MLV	0.89	0.85	0.88	<b>0.87</b>	0.80	0.89

As shown in Figure 4.6a and Figure 4.6b, the correlation between wavelengths acquired in different images at different times shows a high correlation in all wavelengths with the three methods of PSI, MLV and LPC, with an overall value of

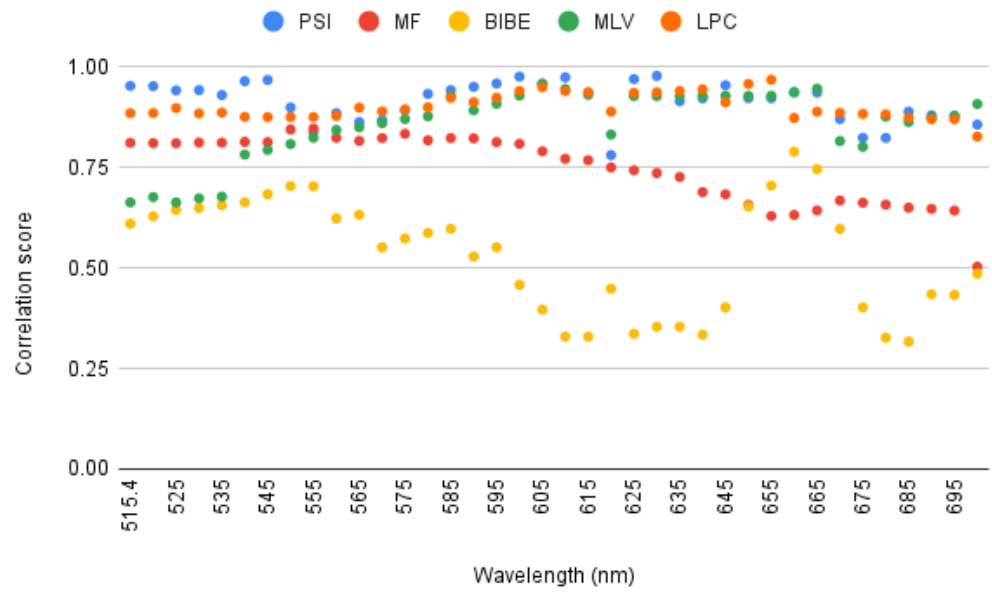
SRCC and PLCC greater than 0.8. As shown in Figure 4.7a and Figure 4.7b, the results in sample 2 shows a good correlation between the wavelengths 700 nm-900 nm, similar to sample 1, but the results in the last region do not show a strong correlation value, particularly between the wavelengths 900 nm-950 nm.

The reason for the low performance in the later wavelength could be due to chromatic aberration which indicates that the light rays flowing through the HSI camera lens are focused at different points depending on the wavelength. According to a study conducted by (Fabelo et al., 2019), low correlation performance in the range 900 nm to 950 nm could also be caused by poor hyperspectral sensor's effectiveness in these spectral bandwidths, as photons have more reflectance energy in the 500 nm-900 nm wavelength range than in the longer wavelength range of 900 nm to 950 nm.

The results also indicates that the system performs better in the spectral bandwidths of 515 nm to 900 nm. Based on the obtained scores of these experimental tests, the optimal spectral bandwidth in which the system can operate with high performance is between 500 nm and 900 nm. Also, since the shortest wavelength bands (500 nm-515 nm) in our sample acquired at KUH contains noises, the bands and the reflectance values in the range between 500 nm to 515 nm were avoided during the HS cube pre-processing and on the parts after sections 4.1.

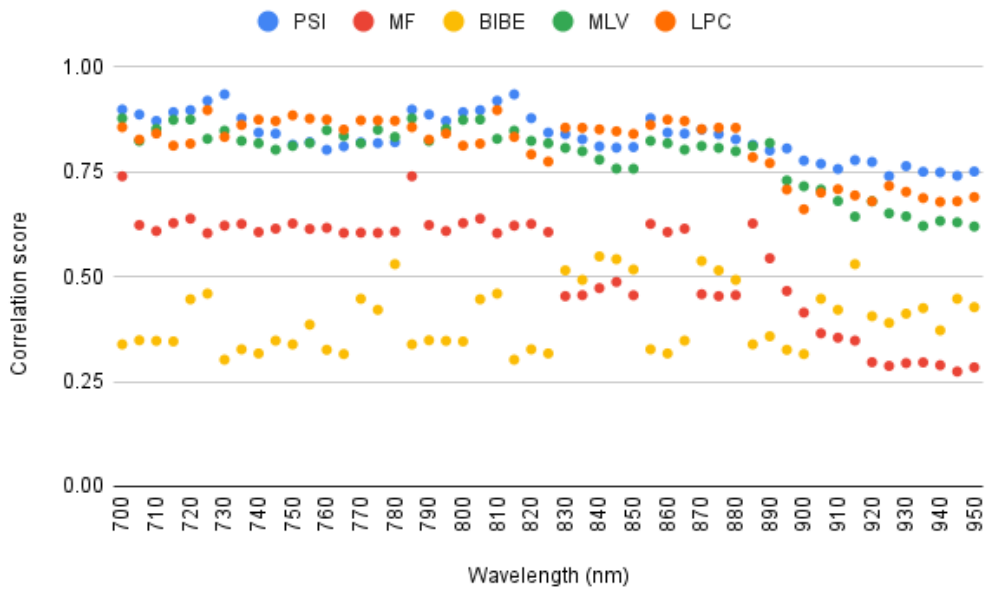


(a) *PLCC*

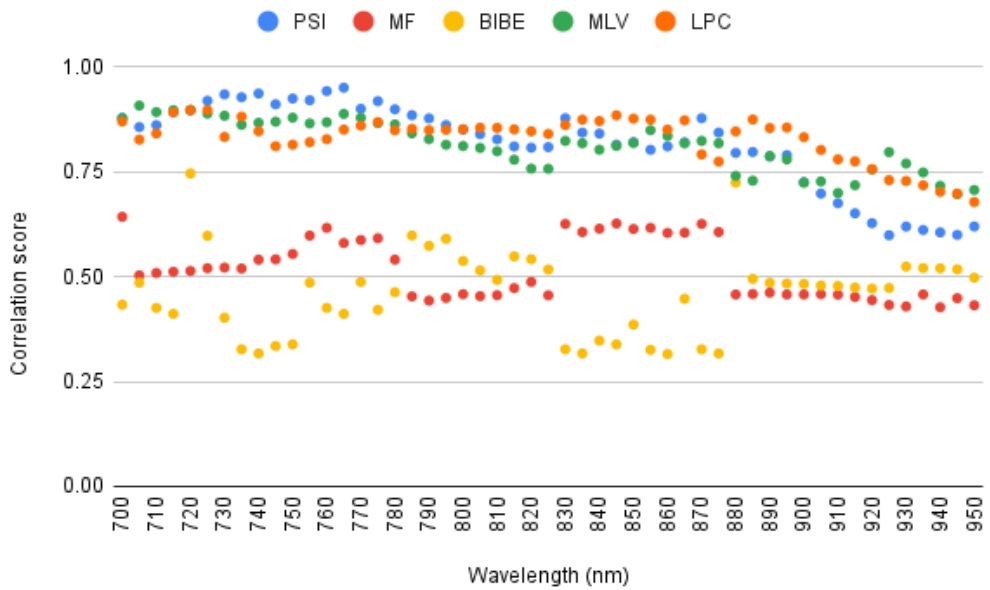


(b) *SRCC*

**Figure 4.6:** Blurriness correlation value vs. wavelength of neurosurgery spectral images using NR-IQA methods. a and b shows PLCC and SRCC results for 515 nm-700 nm respectively.



(a) *PLCC*



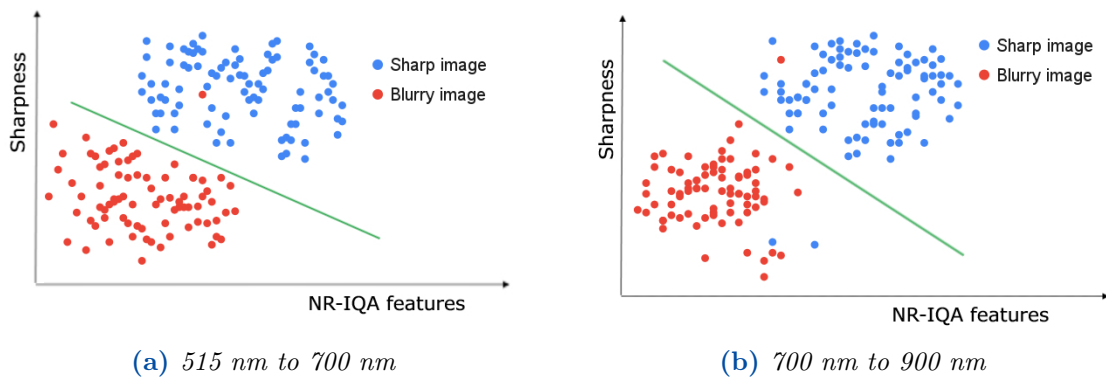
(b) *SRCC*

**Figure 4.7:** Blurriness correlation value vs. wavelength of neurosurgery spectral images using NR-IQA methods. a and b shows PLCC and SRCC results for 700 nm-950 nm respectively.

### 4.3.1 Blur-specific quality estimation with SVM

By removing the band images from 900 nm to 950 nm, two samples in the range of 515 nm to 700 nm and 700 nm to 900 nm are used for SVM classification. Both samples contains good (sharp) images and bad (blurry images). A total of 2248 band images were utilized for classification in each sample, with 20% of the total data used for testing and 80% for training. 25% of the data are labeled as sharp images and 75% of the data are labeled as blurry images, indicating a class imbalanced problem. Six continuous numerical numbers obtained from NR-IQA techniques (results from the NR-IQA methods mentioned above plus a result from the BRISQUE technique) are used as features in the training as a single variable. A discrete variable format is also used to represent the target variable. A discrete variable format is also used to represent the target variable.

Given the presence of outliers in our dataset, the value of  $C$  is expected to be high during model training. For that, we use the soft-margin variant of SVM because the hard-margin variant does not deal with outliers. In this case, a few points may be incorrectly classified. The  $C$  parameter, which regulates outliers, should be used to penalize for each such point since a low  $C$  value implies allowing more outliers while a high  $C$  value implies allowing fewer outliers.



**Figure 4.8:** The classification of the sharp and blurry band images with the SVM model. a) shows the classification of the samples in the range between 515 nm to 700 nm, and b) shows the classification of the samples in the range between 700 nm to 900 nm.

Due to outliers in the dataset, increasing the value of  $C$  to limit fewer outliers has improved accuracy. Maximum accuracy is obtained with rbf and linear kernel with  $C=100.0$ , and the accuracy is 0.985 for sample 1 and 0.928 for sample 2. So, based on the obtained results, we can assume that the model is performing well in



terms of predicting class labels, particularly in sample 1. However, this assumption will not be true for general conclusions to be drawn, and one reason could be the problem of the imbalanced dataset, and also having artificially blurred band images. To reach a general conclusion, the data imbalance issue should be issued, and out-of-focus dataset should be acquired with the HSI camera using the same procedure used to acquire the sharp raw spectral band images rather than creating the blurred images using gaussian blur.

Since accuracy is an insufficient statistic for quantifying prediction ability in this type of data (imbalanced), sensitivity and specificity have also been estimated. Sensitivity, which is determined by the ratio of true positives (TP) to the total of true positives and false negatives (TP + FN), is defined as the proportion of correctly estimated positive outcomes out of all actual positive outcomes. Accordingly, the sensitivity for sample 1 is 0.994, and for sample 2 it is 0.897. Specificity which is defined as the ratio of true negatives correctly predicted by the model, obtained by the ratio of true negatives (TN) to the sum of true negatives and false positives (TN + FP). Accordingly, the specificity for sample 1 is 0.952, while in sample 2 is 0.920.



## 5 | Discussion

The thesis work intends to build a data architecture for hyperspectral imaging database that will be primarily useful for intraoperative microneurosurgical applications with appropriate functionalities to process, store, retrieve, and analyze HSI data. Furthermore, by utilizing NR-IQA techniques, a method for measuring the sharpness of band images acquired with the present hyperspectral imaging equipment was evaluated.

The data architecture now supports adding spectral data in ENVI format, and data uploading to the database is currently only allowed through the database interface, making data addition through the GUI impractical. The data architecture and the designed database are flexible enough to add or remove a class feature, so a new type of tissue or tumor class with its related spectral information can be added to the database. This will ensure that the database has an adequate amount of brain spectral image information that can be used for research work in the machine learning or computer vision-based brain tumor detection or other related topics.

Due to the inherent mobility of the ongoing patient's brain, the ideal spectral device for data acquisition might be snapshot cameras (spectral cameras that can capture both spectral and spatial aspects of a subject with a single shot) that can provide real-time spectral dataset recording. Nevertheless, the volume of spectral band channels in such cameras is ten times smaller than in push-broom cameras. As a result, more studies need to be conducted utilizing hyperspectral images acquired using push-broom devices (better spectral resolution) to determine the important spectral bands that allow the identification of tumor boundaries, and compare the identification results with those obtained using snapshot cameras to create a better gold standard microneurosurgical database.

The Digital Imaging and Communications in Medicine (DICOM) standard, which is an internationally recognized format for viewing, storing, retrieving, and sharing medical images, has previously defined non-proprietary data sharing standards, an imaging data format, and a file system for medical imaging and imaging-related

## Chapter 5 | DISCUSSION

information. But, despite the fact that the standards committee recognizes the necessity, the DICOM standard does not yet contain support for the storing and communication of hyperspectral images. Standards equivalent to RGB image in DICOM are required in HSI data for development of clinically significant intraoperative HSI systems to manage workflow operations and enable image and metadata sharing. As a result, comprehensive interdisciplinary efforts and extensive HSI data gathering are necessary to develop meaningful standardization. When the DICOM committee produces a standards for spectral images in medical domains, particularly microsurgery, the data architecture described in this master thesis should be adjusted to accommodate the data transfer protocol according to the standard.

## 6 | Conclusions

The thesis work objectives was to create a data architecture, database, and working system for an intraoperative application capable of capturing, storing, and processing HS images during neurosurgical procedures. The created database can also be used to provide open access to a public intraoperative HSI database of the human brain, specifically for brain tumor detection in the research community. During surgical procedures at Kuopio University Hospital, Finland, the HS imaging system was used, and in the VNIR (500 nm to 900 nm), 52 images from 10 different patients were acquired. Specialists (neurosurgeons) labeled the obtained HS images to create a highly comprehensive gold standard data set of labeled brain tissue and tumors. The mean spectral signature of labeled brain tissue and tumors was computed and stored in the database which can be used as a reference for tumor and healthy tissue delineation during in vivo brain surgery in complementary with other imaging modalities such as MRI and CT scans.

NR-IQA was applied to two different data sets to assess the sharpness of the hyperspectral images. One covers the wavelength range from 500 nm to 950 nm, while the other covers the wavelength range from 500 nm to 900 nm. The quality evaluation results show that the PSI algorithms perform better for evaluating the sharpness of the band images. The evaluation also revealed that the most efficient spectral range for the system is between 500 nm and 900 nm. Following that, the result indicated that NR-IQA-based blur-specific methods used for RGB-based images could also be used to evaluate the sharpness of band images acquired using a hyperspectral imaging system. Some differences were noticed between the results of the focus assessment using NR-IQA, as the results were more consistent and of better quality only between 500 nm and 900 nm. Furthermore, after applying the assessment methods separately for each wavelength, it was observed that there is a focus difference in the last wavelengths between 900 nm and 950 nm based on the SRCC and PLCC correlation values. Generally, Using the obtained spectral images, the results indicated that blur-specific quality evaluation methodologies introduced for non-spectral images (RGB) could also be used to assess the sharpness of hyperspectral images. Nonetheless, in several of the bands, the dataset revealed

## Chapter 6 | CONCLUSIONS

low correlations in the blur-specific quality of the spectral bands within different images but at identical wavelengths. The reason for this could be camera aberration or the HS sensor's poor performance at those wavelengths (Fabelo et al., 2019).

## 7 | Limitations and Future Works

A comprehensive database that contains all of the possible tumor and tissue types that could be detected in different human patients was unable to be created because of the limited number of neurosurgical spectral images that were gathered. Only 52 neurosurgical hyperspectral images are presently available in the database. In the future, new data sets should be collected and added to the database in order to present a more accurate representation of the spectral signature of various brain tissues and tumors. Additionally, the database includes images obtained with the spectral camera at KUH, and the classes of the spectral images are anatomically labeled by experienced neurosurgeons. However, in order to have a more reliable gold standard dataset and spectral signature representations, it would be preferable to include more brain images taken with different HSI camera models and annotated by multiple experts in the field. This issue should be taken into consideration in the future acquisition of the brain spectral images.

Although the blurred datasets used in this study were artificially blurred using gaussian blur, future work might also focus on capturing additional spectral images with varied depths of focus and a wide wavelength coverage for an accurate evaluation of the spectral band images. I believe that having enough datasets of raw and blurred images will aid in the development of an efficient machine-learning-based focus assessment algorithm to ensure the acquisition of microscopic high quality hyperspectral images that can be used as a gold standard reference for real-time microneurosurgery.

## Chapter 7 | LIMITATIONS AND FUTURE WORKS



# A | Appendix

Home · Imaging\_Database

### Imaging\_Database administration

IMAGING_DATABASE		
Addresss	+ Add	✎ Change
Annotations	+ Add	✎ Change
Average_reflectances	+ Add	✎ Change
Cameras	+ Add	✎ Change
Categorys	+ Add	✎ Change
Class_features	+ Add	✎ Change
Diagnosis_historys	+ Add	✎ Change
Diagnosisiss	+ Add	✎ Change
Environments	+ Add	✎ Change
Hospitals	+ Add	✎ Change
Imagings	+ Add	✎ Change
Light_sources	+ Add	✎ Change

(a)





Masks	+ Add	✎ Change
Metadatas	+ Add	✎ Change
Patients	+ Add	✎ Change
Reflectances	+ Add	✎ Change
Softwares	+ Add	✎ Change
Spectral_images	+ Add	✎ Change
Surgeons	+ Add	✎ Change
Tissue_classss	+ Add	✎ Change

(b)

Figure A.1: Layout of the designed database system. a and b shows sample of the DB

## Change spectral image



005

Category:	<input type="text" value="Brain"/>  
Patient:	<input type="text" value="005"/>  
Raw:	Currently: rawfiles/raw_zE4EaCv.raw Change: <input type="button" value="Choose File"/> No file chosen
Hdr:	Currently: hdrfiles/raw_To7ez1Q.hdr Change: <input type="button" value="Choose File"/> No file chosen
Rgb:	Currently: RGB/image_jBAakK8.jpg Change: <input type="button" value="Choose File"/> No file chosen
Description:	<div style="border: 1px solid #ccc; padding: 5px;"><p>For this patient, the tissue labels are categorized to tissue class, subclass, and class feature. The tissue classes include dura, bone, parenchyma, artery, vein, cranial nerve, ependyma, blood and pathology. The subclasses are class dependent and include superficial and deep for vein class, and glioma, meningioma and aneurysm for pathology class.</p></div>

(a)

## Change imaging

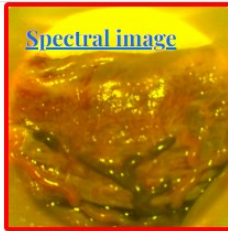

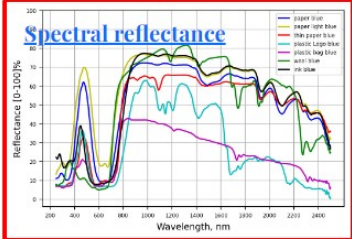
### Spatial scanning

Spectral image:	<input type="text" value="004"/>  
Acquisition type:	<input type="text" value="Spatial scanning"/>
Light intensity:	<input type="text" value="36.0"/>
Magnification:	<input type="text" value="16x"/>
Focal length:	<input type="text" value="54.0"/>

(b)

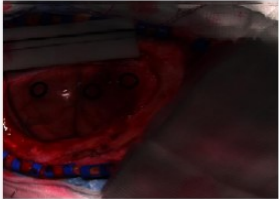
**Figure A.2:** Layout of the designed database system. a and b shows design of interface for adding spectral image and imaging system information respectively. 61

## Neurosurgical Hyperspectral Database

Brain	Spinal cord	Central and peripheral nerve	Cerebral circulation
<p>Common classes</p> <ul style="list-style-type: none"> <li><a href="#">Dura</a></li> <li><a href="#">Artery</a></li> <li><a href="#">Vein</a></li> <li><a href="#">Ependyma</a></li> <li><a href="#">Blood</a></li> </ul>	<p style="background-color: #4CAF50; color: white; padding: 2px;">Class tissue and tumor</p> <div style="border: 1px solid #ccc; padding: 5px; margin-bottom: 5px;"> <input type="text" value="class"/> <input type="button" value="Search"/> </div> <ul style="list-style-type: none"> <li>Dura</li> <li>Artery</li> <li>Ependyma</li> <li>Parenchyma</li> <li>Bone</li> <li>Cranial nerve</li> </ul>	 <p style="color: blue; font-weight: bold;">Spectral image</p>	 <p style="color: blue; font-weight: bold;">Mask and class</p>
		 <p style="color: blue; font-weight: bold;">Spectral reflectance</p>	

(a)

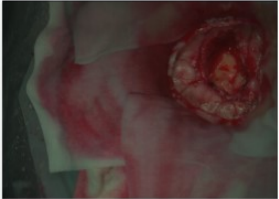
Brain



For this patient the tissue labels are categorized to tissue class, subclass, and class feature. The tissue classes include dura, . . .

[read more](#)

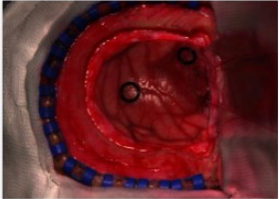
Image Details



For this patient the tissue labels are categorized to tissue class, subclass, and class feature. The tissue classes include dura, . . .

[read more](#)

Image Details



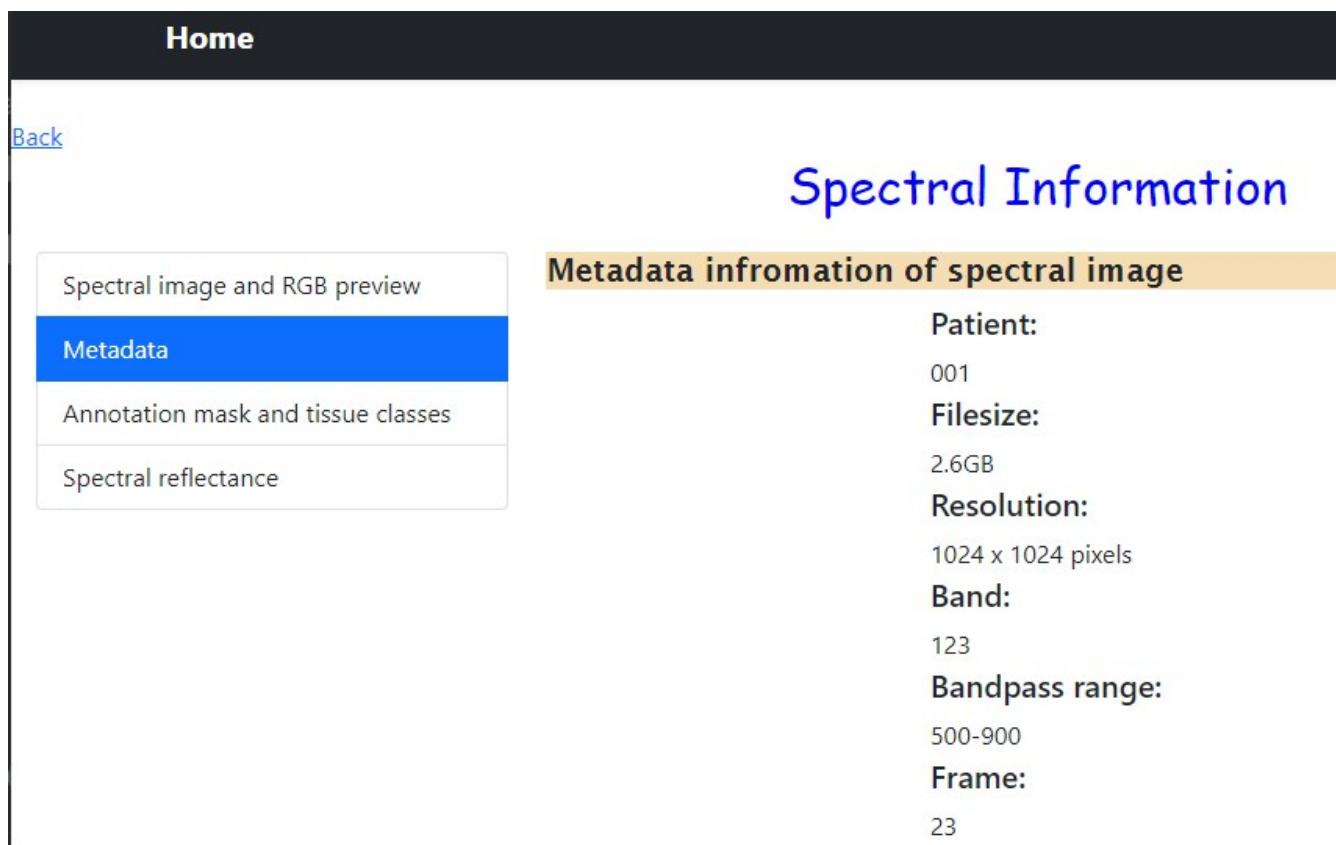
For this patient, the tissue labels are categorized to tissue class, subclass, and class feature. The tissue classes include dura . . .

[read more](#)

Image Details

(b)

**Figure A.3:** Layout of the GUI. a) shows layout of the front page, and b) shows layout of RGB/thumbnail information search page.



(a)

**Figure A.4:** *Layout of the designed GUI for metadata information*



# Bibliography

- Ayala, L., Wirkert, S., Gröhl, J., Herrera, M., Hernandez-Aguilera, A., Vemuri, A., Santos, E., and Maier-Hein, L. (2019). *Live Monitoring of Haemodynamic Changes with Multispectral Image Analysis*, pages 38–46. (cited on page 12)
- Blair, S., García, M., Konopka, C., Dobrucki, W., and Gruev, V. (2019). A 27-band snapshot hyperspectral imaging system for label-free tumor detection during image-guided surgery. page 16. (cited on page 1)
- Bolton, F., Bernat, A., Bar-Am, K., Levitz, D., and Jacques, S. (2018). Portable, low-cost multispectral imaging system: Design, development, validation, and utilization. *Journal of Biomedical Optics*, 23:1. (cited on pages 10 and 12)
- Clancy, N., Jones, G., Maier-Hein, L., Elson, D., and Stoyanov, D. (2020). Surgical spectral imaging. *Medical Image Analysis*, 63:101699. (cited on page 10)
- Dijk, J., van Ginkel, M., Asselt, R., Van Vliet, L., and Verbeek, P. (2003). A new sharpness measure based on gaussian lines and edges. pages 149–156. (cited on page 17)
- Dr. Dr. Dale, L., Thewis, A., Boudry, C., Rotar, I., Dardenne, P., Baeten, V., and Fernández Pierna, J. (2013). Hyperspectral imaging applications in agriculture and agro-food product quality and safety control: A review. *Applied Spectroscopy Reviews*, 48:142. (cited on page 1)
- Du, X., Clancy, N., Arya, S., Hanna, G., Kelly, J., Elson, D., and Stoyanov, D. (2015). Robust surface tracking combining features, intensity and illumination compensation. *International journal of computer assisted radiology and surgery*, 10. (cited on page 10)
- Ebner, M., Nabavi, E., Shapey, J., Xie, Y., Liebmann, F., Spirig, J., Hoch, A., Farshad, M., Saeed, S., Bradford, R., Yardley, I., Ourselin, S., Edwards, D., Fürnstahl, P., and Vercauteren, T. (2021). Intraoperative hyperspectral label-free imaging: From system design to first-in-patient translation. *Journal of Physics D: Applied Physics*, 54. (cited on page 13)

## BIBLIOGRAPHY

- Fabelo, H., Id, S., Ortega, S., Lazcano, R., Id, D., Madroñal, D., Id, G., Marrero Callico, G., Juarez, E., Salvador, R., and Id (2018). An intraoperative visualization system using hyperspectral imaging to aid in brain tumor delineation. *Sensors*, 18. (cited on pages 1 and 13)
- Fabelo, H., Ortega, S., Kabwama, S., Marrero Callico, G., Bulters, D., Szolna, A., Pineiro, J., and Sarmiento, R. (2016). Helicoid project: a new use of hyperspectral imaging for brain cancer detection in real-time during neurosurgical operations. page 986002. (cited on pages 3 and 13)
- Fabelo, H., Ortega, S., Szolna, A., Bulters, D., Pineiro, J., Kabwama, S., J-O´Shanahan, A., Bulstrode, H., Bisshopp, S., Kiran, B., Ravì, D., Lazcano, R., Madroñal, D., Sosa, C., Espino, C., Marquez, M., Plaza, M., Camacho, R., Carrera, D., and Sarmiento, R. (2019). In-vivo hyperspectral human brain image database for brain cancer detection. *IEEE Access*, PP:1–1. (cited on pages 1, 2, 3, 15, 47, and 56)
- Fawzy, Y., Lam, S., and Zeng, H. (2015). Rapid multispectral endoscopic imaging system for near real-time mapping of the mucosa blood supply in the lung. *Biomedical optics express*, 6:2980–90. (cited on page 12)
- Feichtenhofer, C., Fassold, H., and Schallauer, P. (2013). A perceptual image sharpness metric based on local edge gradient analysis. *IEEE Signal Processing Letters*, 20:379–382. (cited on page 28)
- Gandhe, R. and Bhave, C. (2018). Intraoperative magnetic resonance imaging for neurosurgery - an anaesthesiologist’s challenge. *Indian Journal of Anaesthesia*, 62:411–417. (cited on page 2)
- Gebejes, A., Fält, P., Bednarik, R., and Hauta-Kasari, M. (2016). Speed: Spectral eye video database. pages 1666–1675. (cited on pages 3 and 15)
- Hagen, N. and Kudenov, M. (2013). Review of snapshot spectral imaging technologies. *Optical Engineering*, 52:090901. (cited on page 11)
- Hassen, R., Wang, Z., and Salama, M. (2013). Image sharpness assessment based on local phase coherence. *IEEE transactions on image processing : a publication of the IEEE Signal Processing Society*, 22. (cited on page 32)
- Hauta-Kasari, M., Lehtonen, J., Parkkinen, J., and Jääskeläinen, T. (2006). Image format for spectral image browsing. *Journal of Imaging Science and Technology - J IMAGING SCI TECHNOL*, 50. (cited on page 14)



## BIBLIOGRAPHY

- Hege, K., O’Connell, D., Johnson, W., Basty, S., and Dereniak, E. (2004). Hyperspectral imaging for astronomy and space surveillance. *Proceedings of SPIE - The International Society for Optical Engineering*, 5159. (cited on page 1)
- Holmer, A., Marotz, J., Wahl, P., Dau, M., and Kaemmerer, P. (2018). Hyperspectral imaging in perfusion and wound diagnostics - methods and algorithms for the determination of tissue parameters. *Biomedical Engineering / Biomedizinische Technik*, 63. (cited on page 10)
- Hou, R., Hu, Y., Zhao, Y., and Liu, H. (2020). Hyperspectral image quality evaluation using generalized regression neural network. *Signal Processing: Image Communication*, 83:115785. (cited on page 16)
- Hubel, D. and Wiesel, T. (1998). Early exploration of the visual cortex. *Neuron*, 20:401–12. (cited on pages 30 and 31)
- Hyttinen, J., Fält, P., Jäsberg, H., Kullaa, A., and Hauta-Kasari, M. (2020). Oral and dental spectral image database—odsi-db. *Applied Sciences*, 10:7246. (cited on pages 3 and 15)
- Jansen-Winkel, B., Holfert, N., Köhler, H., Moulla, Y., Takoh, J., Rabe, S., Mehdorn, M., Barberio, M., Chalopin, C., Neumuth, T., and Gockel, I. (2019). Determination of the transection margin during colorectal resection with hyperspectral imaging (hsi). *International Journal of Colorectal Disease*, 34. (cited on page 3)
- Kiyotoki, S., Nishikawa, J., Okamoto, T., Hamabe, K., Saito, M., Goto, A., Fujita, Y., Hamamoto, Y., Takeuchi, Y., Satori, S., and Sakaida, I. (2013). New method for detection of gastric cancer by hyperspectral imaging: A pilot study. *Journal of biomedical optics*, 18:26010. (cited on page 12)
- Kumar, J., Chen, F., and Doermann, D. (2012). Sharpness estimation for document and scene images. pages 3292–3295. (cited on page 32)
- Li, D. and Jiang, T. (2019). *Blur-Specific No-Reference Image Quality Assessment: A Classification and Review of Representative Methods*, pages 45–68. (cited on page 28)
- Li, L., Lin, W., Wang, X., Yang, G., Bahrami, K., and Kot, A. (2015a). No-reference image blur assessment based on discrete orthogonal moments. *IEEE transactions on cybernetics*, 46. (cited on page 16)
- Li, L., Lin, W., Wang, X., Yang, G., Bahrami, K., and Kot, A. (2015b). No-reference image blur assessment based on discrete orthogonal moments. *IEEE transactions on cybernetics*, 46. (cited on page 31)

## BIBLIOGRAPHY

- Li, Q., He, X., Wang, Y., Liu, H., Xu, D., and Guo, F. (2013). Review of spectral imaging technology in biomedical engineering: Achievements and challenges. *Journal of biomedical optics*, 18:100901. (cited on page 24)
- Lin, J., Clancy, N., Qi, J., Hu, Y., Tatla, T., Stoyanov, D., Maier-Hein, L., and Elson, D. (2018). Dual-modality endoscopic probe for tissue surface shape reconstruction and hyperspectral imaging enabled by deep neural networks. *Medical Image Analysis*, 48. (cited on page 12)
- Lu, G. and Fei, B. (2014). Medical hyperspectral imaging: A review. *Journal of biomedical optics*, 19:10901. (cited on pages 2 and 9)
- Ma, Y., Shaik, M., Kim, S., Kozberg, M., Thibodeaux, D., Zhao, H., Yu, H., and Hillman, E. (2016). Wide-field optical mapping of neural activity and brain haemodynamics: Considerations and novel approaches. *Philosophical Transactions of the Royal Society B: Biological Sciences*, 371. (cited on pages 10 and 12)
- Marcello, P., Cucci, C., Casini, A., and Stefani, L. (2020). Hyper-spectral imaging technique in the cultural heritage field: New possible scenarios. *Sensors*, 20:2843. (cited on page 1)
- Marziliano, P., Dufaux, F., Winkler, S., and Ebrahimi, T. (2002). A no-reference perceptual blur metric. volume 53, pages III–57. (cited on page 16)
- Meer, F., van der Werff, H., Ruitenbeek, F., Hecker, C., Bakker, W., Noomen, M., Meijde, M., Carranza, E. J., de Smeth, B., and Woldai, T. (2012). Multi-and hyperspectral geologic remote sensing: A review. *International Journal of Applied Earth Observation and Geoinformation*, 14:112–128. (cited on page 16)
- Ortega, S., Fabelo, H., Iakovidis, D., Koulaouzidis, A., and Marrero Callico, G. (2019a). Use of hyperspectral/multispectral imaging in gastroenterology. shedding some–different–light into the dark. *Journal of Clinical Medicine*, 8:36. (cited on page 3)
- Ortega, S., Guerra Hernández, R., Diaz, M., Fabelo, H., Lopez, S., Marrero Callico, G., and Sarmiento, R. (2019b). Hyperspectral push-broom microscope development and characterization. *IEEE Access*, PP:1–1. (cited on page 3)
- Ortega, S., Halicek, M., Fabelo, H., Camacho, R., Plaza, M., Godtlielsen, F., Marrero Callico, G., and Fei, B. (2020). Hyperspectral imaging for the detection of glioblastoma tumor cells in h&e slides using convolutional neural networks. *Sensors*, 20:1911. (cited on page 3)

## BIBLIOGRAPHY

- Pichette, J., Charle, W., and Lambrechts, A. (2017). Fast and compact internal scanning cmos-based hyperspectral camera: the snapsan. page 1011014. (cited on page 10)
- Pisani, M., Zucco, M., Caricato, V., and Egidi, A. (2013). Hyperspectral imaging: a tool for biological measurements. (cited on page 1)
- Polder, G. and Gowen, A. (2020). The hype in spectral imaging. *Journal of Spectral Imaging*, 9(1):a4. (cited on page 9)
- Puustinen, S., Hyttinen, J., Hisuin, G., Vrzakova, H., Huotarinen, A., Fält, P., Hauta-Kasari, M., Immonen, A., Koivisto, T., Jääskeläinen, J. E., and Elomaa, A.-P. (2022). Towards clinical hyperspectral imaging (hsi) standards: Initial design for a microneurosurgical hsi database. (cited on pages 6, 19, 20, 22, 23, 24, and 71)
- Quintana Quintana, L., Ortega, S., Fabelo, H., and Marrero Callico, G. (2021). Blur-specific no-reference image quality assesment for microscopic hyperspectral image focus quantification. pages 1–5. (cited on page 16)
- Ruiz, L., Martin, A., Urbanos, G., Villanueva, M., Sancho, J., Rosa, G., Villa, M., Chavarrías, M., Perez, A., Juarez, E., Lagares, A., and Sanz, C. (2020). Multiclass brain tumor classification using hyperspectral imaging and supervised machine learning. pages 1–6. (cited on page 13)
- Sakamoto, J., Dumont, J., Fauch, L., Keski-Saari, S., Granlund, L., Porali, I., Orava, J., Hiltunen, J., Oksanen, E., Keinänen, M., and Hauta-Kasari, M. (2014). Natural vision data file format as a new spectral image format for biological applications. volume 8509, pages pp 124–132. (cited on page 14)
- Styles, I., Calcagni, A., Claridge, E., Orihuela-Espina, F., and Gibson, J. (2006). Quantitative analysis of multi-spectral fundus images. *Medical image analysis*, 10:578–97. (cited on page 3)
- Sun, T., Zhu, X., Pan, J.-S., Wen, J., and Meng, F. (2015). No-reference image quality assessment in spatial domain. *Advances in Intelligent Systems and Computing*, 329:381–388. (cited on page 16)
- Tetschke, F., Markgraf, W., Gransow, M., Kromnik, S., Thiele, C., Kulcke, A., and Malberg, H. (2016). Hyperspectral imaging for monitoring oxygen saturation levels during normothermic kidney perfusion. *Journal of Sensors and Sensor Systems*, 5:313–318. (cited on page 12)

## BIBLIOGRAPHY

- Wang, S., Deng, C., Zhao, B., Huang, G.-B., and Wang, B. (2015). Gradient-based no-reference image blur assessment using extreme learning machine. *Neurocomputing*, 174. (cited on page 33)
- Wang, Y., Reder, N., Kang, S., Glaser, A., and Liu, J. (2017). Multiplexed optical imaging of tumor-directed nanoparticles: A review of imaging systems and approaches. *Nanotheranostics*, 1:369–388. (cited on pages 11 and 71)
- Wang, Z., Bovik, A., and Evan, B. (2000). Blind measurement of blocking artifacts in images. volume 3, pages 981 – 984 vol.3. (cited on page 17)
- Yamaguchi, M., Hauta-Kasari, M., Herzog, P., Derhak, M., Hardeberg, J., Helling, S., Hernández-Andrés, J., Hill, B., Hung, P.-C., Imai, F., Lenz, R., Miyake, Y., Morovic, P., Shyu, M., and Parkkinen, J. (2017). Cie 223:2017 multispectral image formats. (cited on page 14)
- Yan, Q., Xu, Y., and Yang, X. (2013). No-reference image blur assessment based on gradient profile sharpness. In *2013 IEEE International Symposium on Broadband Multimedia Systems and Broadcasting (BMSB)*, pages 1–4. (cited on page 17)
- Yoon, J., Joseph, J., Waterhouse, D., Luthman, S., Gordon, G., di Pietro, M., Januszewicz, W., Fitzgerald, R., and Bohndiek, S. (2019). A clinically translatable hyperspectral endoscopy (hyse) system for imaging the gastrointestinal tract. *Nature Communications*, 10. (cited on page 10)
- Yuen, P. and Richardson, M. (2010). An introduction to hyperspectral imaging and its application for security, surveillance and target acquisition. *Imaging Science Journal, The*, 58:241–253. (cited on page 1)

# List of Figures

1.1	a) Data cube representation b) RGB representation. The data cube contains spatial and spectral data. On the left is a pixel’s spectral reflectance curve. On the right, the RGB representation contains three bands for red, green, and blue wavelengths, and a pixel’s intensity curve from the RGB scene. . . . .	2
2.1	Methods for collecting hyperspectral images. Both A and B illustrate spatial scanning. Scan Point (A). Line scan (B). spectral scanning (C). Snapshot (D). Adapted from (Wang et al., 2017) . . . . .	11
3.1	Flowchart for the use of HSI systems in neurosurgical applications, including the collecting of hyperspectral data during the removal of brain tumors. The imaging process in neurosurgery may be broken down into three distinct phases: preoperative, intraoperative, and postoperative. The data flow that is being managed between the three phases is shown by the red arrow. hyperspectral imaging camera (1), microscope (surgical) (2), light source (3). . . . .	21
3.2	The intraoperative system utilized for hyperspectral data collection. (A) the laptop used to manage the HSI acquisition, (B) the surgical tower, (C) the operation microscope, (D) the HSI camera, (E) the neuronavigation monitor, (F) the monitor displaying the field of view of the operation microscope, and (G) the patient. (Puustinen et al., 2022) . . . . .	22
3.3	The VNIR hyperspectral image’s most representative bands (515 nm to 900 nm) from the database of patient-1 . . . . .	23
3.4	White and dark correction workflow. . . . .	25
3.5	Binary mask representations of the in-vivo hyperspectral human brain image database. The patient and image identification (ID) are represented by the numeric code seen above each image (PatientID-ImageID). The colored regions denote the position of various labeled brain tissue and tumors. . . . .	26

## LIST OF FIGURES

3.6	Raw RGB and band images with their corresponding blurred images a) RGB and band images acquired at KUH b) RGB and band images with gaussian blur (sigma =1) c) RGB and band images with gaussian blur (sigma =3) d) RGB and band images with gaussian blur (sigma =4). Rows 1 and 2 belong to patient 1 in the database, whereas rows 3 and 4 belong to patient 4 in the database. . . . .	29
3.7	A comprehensive categorization of blur-specific, no-reference image quality evaluation techniques, including learning-free and learning-based techniques. . . . .	30
3.8	Flowchart of NSS-based BIBE method . . . . .	34
3.9	Hyperplanes in SVM . . . . .	34
4.1	Designed data architecture for the microneurosurgical HSI database, illustrating data model relationships. Crow's foot notation is used to represent one-to-one, one-to-many, and many-to-many relationships between models. . . . .	40
4.2	Reflectance properties of tissue and tumor classes from the GUI. . .	41
4.3	a) RGB reference image of an operation microscope b) The associated HSI mask of patient ID 0003 with labeled healthy tissue and tumor areas. Anatomical annotations provide localizing information, while tissue labels delineate the relevant features for the HSI analysis. . .	43
4.4	The mean and standard deviation spectral signatures of different tissue and tumor type across all patients in the database between 500 nm to 900 nm wavelength range. Using feature scaling, the reflectance values are normalized to between 0 and 1. (a) Artery intracranial; (b) Blood; (c) Bone compact; (d) Dura internal; (e) Glioblastoma; (f) Grey matter with pia. . . . .	44
4.5	Mean spectral reflectance for different class tissues from the gold standard spectral images in the database. . . . .	45
4.6	Blurriness correlation value vs. wavelength of neurosurgery spectral images using NR-IQA methods. a and b shows PLCC and SRCC results for 515 nm-700 nm respectively. . . . .	48
4.7	Blurriness correlation value vs. wavelength of neurosurgery spectral images using NR-IQA methods. a and b shows PLCC and SRCC results for 700 nm-950 nm respectively. . . . .	49
4.8	The classification of the sharp and blurry band images with the SVM model. a) shows the classification of the samples in the range between 515 nm to 700 nm, and b) shows the classification of the samples in the range between 700 nm to 900 nm. . . . .	50

## LIST OF FIGURES

A.1	Layout of the designed database system. a and b shows sample of the DB . . . . .	60
A.2	Layout of the designed database system. a and b shows design of interface for adding spectral image and imaging system information respectively. . . . .	61
A.3	Layout of the GUI. a) shows layout of the front page, and b) shows layout of RGB/thumbnail information search page. . . . .	62
A.4	Layout of the designed GUI for metadata information . . . . .	63

## LIST OF FIGURES



# List of Tables

- 2.1 A comparison of existing surgical spectral imaging approaches. . . . 12
- 4.1 Correlation results with different approaches. Bold scores indicate a better assessment outcome when compared to the other approaches. 46